arXiv:1604.07308v1 [physics.flu-dyn] 25 Apr 2016

OBLIQUE CHAIN RESONANCE OF INTERNAL WAVES BY THREE-DIMENSIONAL SEABED CORRUGATIONS

L.-A. COUSTON, Y. LIANG, & M.-R. ALAM

Department of Mechanical Engineering, University of California, Berkeley

Abstract. Here we show that the interaction of a low-mode internal wave with small oblique seabed corrugations can trigger the formation of many other internal waves with a broad range of wavenumbers and directions of propagation. We show that the wave-seabed resonance in a continuously stratified fluid, in contrast to homogeneous and two-layer fluids, is not limited to only one new resonant wave but that it can lead to a chain resonance of many freely propagating waves. The development of chain resonance results in a complex internal wave dynamics over the corrugated seabed that can lead to a significant redistribution of energy across the internal wave spectrum. In order to obtain a quantitative understanding of the energy transfer rates between the incident and resonated waves over the seabed topography, here we derive an equation for the evolution of the wave envelopes using multiple-scale analysis in the limit of small-amplitude corrugations. Strong energy transfers from the incident internal wave toward shorter internal waves are demonstrated for a broad range of incidence angles, and the theoretical predictions are compared favorably with direct simulations of the full Euler's equation. The key results show that: (i) a large number of distinct internal waves can be simultaneously resonated for almost all angles of the seabed corrugations, (ii) near-resonance waves may play a major role in the overall dynamics and hence cannot be ignored, and (iii) near-resonance waves can even sometimes dominate the internal wave field–a phenomenon known as *enhanced detuned resonance*. The chain resonance of internal waves with topography occurs for a wide range of physical conditions including those representatives of the continental shelf or the abyss. The chain resonance of internal waves via single seabed harmonic may, therefore, be one of the select pathways toward efficient enhanced diapycnal mixing and energy dissipation in the real ocean.

1. Introduction

The evolution and fate of internal waves in the ocean is of significant contemporary interest because the current and future state of the climate is believed to be intimately related to the ocean internal wave dynamics and to their role in turbulent processes (*Schiermeier*, 2007; *Mackinnon*, 2013; *DeCarlo et al.*, 2015). Internal waves that are sufficiently steep or in the act of breaking indeed contribute to the mixing and energy dissipation of the ocean, hence to the overall energy balance (c.f. *Wunsch and Ferrari*, 2004; *Nikurashin and Ferrari*, 2013). A significant fraction of the internal waves at their generation site often have long wavelengths (*Garrett and St Laurent*, 2002; *Alford et al.*, 2016). A steepening mechanism must therefore take place during the propagation of internal waves to explain the observed high levels of turbulence and ocean mixing (*Wunsch and Ferrari*, 2004). The process of steepening comes from energy transfers across the internal wave spectrum. It can result from a number of processes including nonlinear wave-wave interactions, wave-mean flow interactions, and bottom scattering (*Garrett and Munk*, 1979; *Staquet and Sommeria*, 2002). The effect of the variable seabed, which is the focus of this study, is elaborated on in the next sections.

The interaction of oceanic flows with variable bottom topography on the continental shelf and in the open ocean is known to be at the origin of enhanced mixing and to be responsible for maintaining the global oceanic circulation (*Munk and Wunsch*, 1998; *Mackinnon*, 2013). Numerical experiments and field measurements have shown that large internal waves interacting at topography can contribute as a source of turbulent kinetic energy in shallow water (e.g. *Kranenburg et al.*, 1991; *Pietrzak et al.*, 1991; *Baines*, 1997; *Pietrzak and Labeur*, 2004; *Labeur and Pietrzak*, 2004), but also in the abyss, where intense vertical mixing (by orders of magnitude) over rough topographies have been observed (*Polzin et al.*, 1997; *Garabato et al.*, 2004), with attribution to internal wave breaking (e.g. *Ledwell et al.*, 2000). In the deep ocean, an important source of internal wave energy comes from the interaction of topographic features with barotropic tides and

E-mail address: louisalexandre.couston@berkeley.edu, yliang1213@berkeley.edu, reza.alam@berkeley.edu.

geostrophic flows (*Garrett and Kunze*, 2007; *Nikurashin and Ferrari*, 2010; *Alford et al.*, 2016). Internal waves generated at topography in the deep ocean typically have long wavelengths (low mode) when they are first generated, and are able to propagate over long distances within the ocean basin (*St Laurent and Garrett*, 2002), as observed for instance northeast of Hawaii (*Zhao et al.*, 2010). The subsequent steepening of these waves interacting nonlinearly or with other seabed topography is of significant interest in order to understand how the energy available for ocean mixing can be redistributed far from the abyssal generation sites (*St Laurent and Garrett*, 2002; *Alford*, 2003). It should be noted that the effect of the dissipating internal waves on the mean-flow that generated them at seabed topography is also of importance, though it has gained interest only relatively recently (see e.g. *Grisouard and Bühler*, 2012).

The seafloor topography includes both relatively large deterministic features, as well as rough patches of small corrugations (*St Laurent and Garrett*, 2002; *Garrett and Kunze*, 2007). Large seafloor topography are usually well resolved by bathymetry measurements (*Mathur et al.*, 2014; *Legg*, 2014), and the process by which they can lead to significant mixing, due to e.g. wave breaking at critical slopes, can be analyzed in details (*Lamb*, 2014). Deterministic analytical methods based on e.g. Green's functions, for instance, have been employed to show that the interaction of the barotropic tide with idealized topography can lead to the development of instability regions in three dimensions where generated internal waves may produce significant turbulence (*Bühler and Muller*, 2007). Extended patches of small seabed variations, on the other hand, are typically represented as continuous bathymetry spectra (*Bell*, 1975; *Goff and Jordan*, 1988), with some uncertainty on length scales of $\mathcal{O}(10\text{km})$ and smaller due to lack of resolution (*Melet et al.*, 2013; *Lefauve et al.*, 2015). These are often studied statistically or as random processes (see e.g. *Muller and Bühler*, 2009). Nonetheless, they similarly contribute to the wave scattering particularly in the abyss (*Munk and Wunsch*, 1998). For instance, in two dimensions, the occurrence of internal wave attractors toward which waves are geometrically focused has been demonstrated over random seabed variations, which suggests that zones with locally intense mixing can take place over small-scale seabed topography (*Guo and Holmes-Cerfon*, 2016). In three dimensions, similar results indicative of wave steepening were obtained for rough patches of small corrugations, which were shown to redistribute the energy of incident internal wave spectra toward higher wavenumbers (*Müller and Xu*, 1992). Investigations of wave scattering using continuous topography spectra have been successful in explaining field observations of enhanced mixing (see e.g. *Polzin*, 2004). However, the statistical approach usually assumes horizontal homogeneity and overlooks the details of energy transfers since it focuses on the collective effect of topography. The contribution from each seabed harmonic (with wavenumber vector $\mathbf{k}_b$), which interacts resonantly with an internal wave with wavenumber $\mathbf{k}$ provided that the sum or difference wavenumber $\mathbf{k} \pm \mathbf{k}_b$ is the wavenumber of a free wave, cannot be disentangled from the overall effect. Yet, as will be shown here, even one single bottom harmonic can resonate many triads in a stratified fluid, with potentially significant consequences on the internal wave dynamics.

In a relatively recent investigation of wave focusing in one horizontal dimension, *Bühler and Holmes-Cerfon* (2011), in agreement with earlier analyses of tidal conversion (c.f. *Balmforth et al.*, 2002; *Garrett and Kunze*, 2007), demonstrated that the interaction of an incident internal tide (wavenumber k_1) with a single bottom harmonic (wavenumber k_b) can resonate a series of shorter internal waves, provided that k_b/k_1 is an integer. Under rigid-lid assumption and in a linearly-stratified fluid, all internal wave wavenumbers are indeed integer multiples of k_1 such that each successively resonated wave k_j, starting with $k_2 = k_1 + k_b = 2k_1$ for $k_b = k_1$, can resonate other new higher-wavenumber internal waves $k_{j+1} = k_j + k_b$. The number of resonated waves is infinite, and the successive resonance are shown to result in a monotonous decay of the incident internal tide energy over the corrugations (*Bühler and Holmes-Cerfon*, 2011). The effect of a single bottom harmonic in a continuously stratified fluid is clearly much more complex than in a homogeneous or two-layer fluid. There, the resonant wave-bottom interactions, which are commonly known as Bragg reflection or resonance because they involve two freely propagating wave and one medium wave (i.e. the seabed undulations here), produce only one isolated resonant triad with well explored properties of energy transfers (e.g. *Davies*, 1982; *Mei*, 1985; *Alam et al.*, 2009a). Internal waves in a continuously stratified fluid over seabed topography, on the other hand, can exhibit more intricate dynamics of potentially new physical interest because of the large number of triads that may be coupled through the same bottom harmonic.

Here we are concerned with the problem of internal wave scattering by monochromatic seabed corrugations in a finite-depth ocean, and in three dimensions. The occurrence of chain resonance in a linearly-stratified ocean is the central theme of the present paper, with the emphasis laid for the first time on incident internal waves impinging on oblique corrugations. The problem is motivated by the one-dimensional chain resonance

discussed in *Bühler and Holmes-Cerfon* (2011), as well as by recent field observations which showed that wave-bottom interactions can differ substantially in one and two horizontal dimensions (e.g. *Buijsman et al.*, 2014). We consider perfectly resonant wave-bottom interactions, but also wave-bottom interactions that are only near resonance, i.e. such that the forced wavenumber is not exactly an internal wave wavenumber. Near-resonance interactions (also known as detuned resonance) are of increasing interest in nonlinear wave science (*Tobisch*, 2016), and will be shown to be essential in the present analysis. Because the demonstration of one-dimensional chain resonance in *Bühler and Holmes-Cerfon* (2011) relies on the method of characteristics and a streamfunction formulation, which is not readily applicable in three dimensions, another approach is required. Specifically, here, to predict how strongly the incident and resonated waves interact, we derive an evolution equation for the envelope amplitudes using the method of multiple scales in the weak-topography limit. The method has been successfully applied for many investigations of Bragg resonance in homogeneous water (e.g. *Mei*, 1985), including shore protection (*Yu and Mei*, 2000a), sandbar formation (*Yu and Mei*, 2000b), wave lensing (*Elandt et al.*, 2014), and in two-layer density stratified fluids (*Alam et al.*, 2009b) with applications in the attenuation of long interfacial waves by random bathymetry (*Alam and Mei*, 2007) and broadband cloaking (*Alam*, 2012). Multiple-scale methods have also been employed in studies of wave dynamics in stratified fluids, including weakly nonlinear wave-mean flow interactions at topography (*Nikurashin and Ferrari*, 2010) and the scattering of internal tides by irregular bathymetry (*Li and Mei*, 2014).

The outline of the paper is as follows. In §2, we characterize the different waves involved in chain resonance for oblique corrugations, and we define a detuning parameter for each of the near-resonance interactions. In §3, we provide the derivation details for the multiple-scale equation and give the solution method for the boundary-value problem. In §4, we discuss the variations of the incident and resonated wave amplitudes over the corrugations for a wide range of corrugation angles. In §5, we summarize the key results and conclude.

2. Problem formulation

2.1. **Governing equation and the dispersion relation.** Consider the propagation of waves in an inviscid, incompressible, adiabatic and stably stratified fluid of density $\rho(x,y,z,t)$, bounded by a free surface on the top and a solid seafloor with a mean depth h at the bottom. We take a Cartesian coordinate system with x and y axes on the mean free surface and z axis positive upward ($\hat{x},\hat{y},\hat{z}$ the unit vectors). The equations governing the evolution of the velocity vector $\mathbf{u}=\{u,v,w\}$, density ρ, pressure p and surface elevation η under Boussinesq and f-plane approximations read

$$\rho_0 D_t\mathbf{u} = -\rho_0 f\hat{z}\times\mathbf{u} - \nabla p - \rho g\nabla z,\ -h+b<z<\eta \tag{2.1a}$$

$$D_t\rho = 0,\ -h+b<z<\eta \tag{2.1b}$$

$$\nabla\cdot\mathbf{u} = 0,\ -h+b<z<\eta \tag{2.1c}$$

$$\eta_t = \mathbf{u}\cdot\nabla(z-\eta),\ z=\eta \tag{2.1d}$$

$$D_t p = 0,\ z=\eta \tag{2.1e}$$

$$\mathbf{u}\cdot\nabla(z+h-b) = 0,\ z=-h+b \tag{2.1f}$$

where g is the gravitational acceleration and f the Coriolis frequency. The seafloor position, given by $z=-h+b(x,y)$, is written as a superposition of small bottom irregularities b on the mean slowly-varying seabed h. The total density is $\rho=\bar{\rho}(z)+\rho'(x,y,z,t)$ with $\bar{\rho}(z)$ the background (unperturbed) density and $\rho_0=\bar{\rho}(z=\eta)$ the density on the free surface. The material derivative operator is denoted by D_t and ∇ is the three-dimensional gradient. Equation (2.1a) is the momentum equation (Euler's equations), (2.1b) is an energy equation (*Gill*, 1982), and (2.1c) is the continuity equation. The problem is a well-posed initial-boundary-value problem in the sense that we have five field equations for five unknown variables ($\mathbf{u}$, p and ρ) with appropriate boundary conditions (2.1d)-(2.1f) on the free surface and seabed.

Here we are concerned with small perturbations of the quiescent state, i.e. $\nabla\vec{u}\sim\nabla\rho'\ll\mathcal{O}(1)$, such that we consider the linearized form of the governing equations (2.1), i.e.

$$\left[(\partial_t^2+f^2)\nabla^2+(N^2-f^2)\nabla_H^2\right]w = 0,\ -h\le z\le 0, \tag{2.2a}$$

$$\left[(\partial_t^2+f^2)\partial_z - g\nabla_H^2\right]w = 0,\ z=0, \tag{2.2b}$$

$$w = u\partial_x(b-h)+v\partial_y(b-h),\ z=-h+b, \tag{2.2c}$$

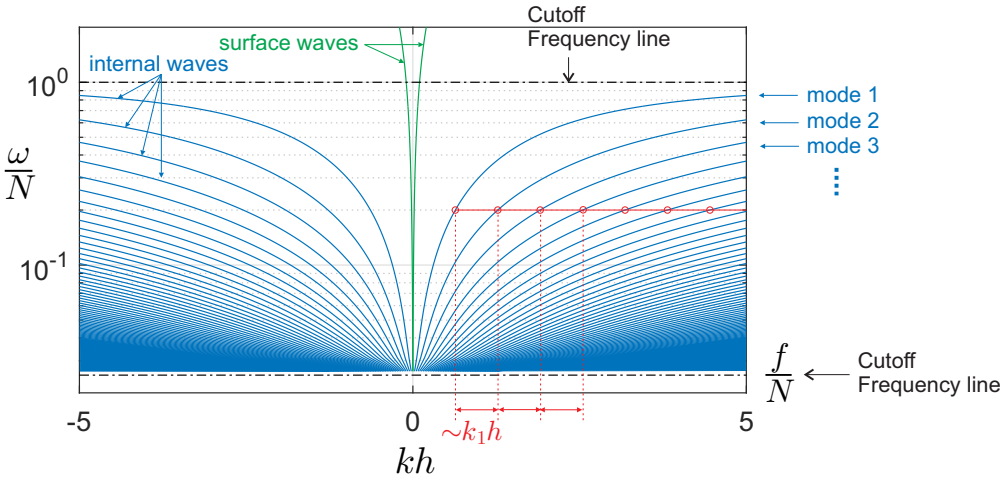

FIGURE 1. Dimensionless frequency ω/N versus dimensionless wavenumber kh of free waves in a linearly stratified fluid with density $\rho(z) = \rho_0(1-az)$, where $ah = 0.01$ and $f/N = 0.025$ (c.f. (2.9)). There is a single surface wave solution at all frequencies $\omega > f$ (solid lines close to y axis) and an infinite number of internal waves (all others) at wave frequencies larger than the Coriolis frequency f and smaller than the Brunt-Väisälä frequency N (i.e. between the dash-dotted cutoff frequency lines). The internal wave wavenumbers are almost uniformly spaced such that $(k_{j+1} - k_j) \sim k_1$ for all $j \geq 1$ at fixed frequency, as highglighted for $\omega/N = 0.2$.

which is derived from (2.1) in Appendix A. We note ∇_H the two-dimensional horizontal gradient and $N = \sqrt{-g/\rho_0[\mathrm{d}\bar{\rho}(z)/\mathrm{d}z]}$ the buoyancy frequency (aka Brunt-Väisälä frequency). Let us consider seabed corrugations of the form

$$b = \frac{d}{2}\left[e^{i(\mathbf{k}_b\cdot\mathbf{x}+\varphi_b)} + e^{-i(\mathbf{k}_b\cdot\mathbf{x}+\varphi_b)}\right], \tag{2.3}$$

where $\mathbf{k}_b = k_b(\cos\theta_b, \sin\theta_b)$ is the corrugation wavenumber with θ_b the corrugation angle, $d > 0$ the corrugation amplitude, and φ_b a phase parameter. For small corrugation amplitude $d/h \sim \mathcal{O}(\epsilon)$ where $\epsilon \ll 1$ is the smallness parameter, the solution w of equation (2.2) can be sought as a perturbation series of the form

$$w = w^{(1)} + w^{(2)} + ... \tag{2.4}$$

where the perturbation terms $w^{(j)} \sim \mathcal{O}(1)$ satisfy the same field equation (2.2a) and top free-surface boundary condition (2.2b). The bottom boundary condition (2.2c), on the other hand, can be rewritten at successive orders in ϵ such that we have at leading order

$$w^{(1)} = 0, \ z = -h, \tag{2.5}$$

and at second order

$$w^{(2)} = u^{(1)}\partial_x b + v^{(1)}\partial_y b - b\partial_z w^{(1)}, \ z = -h, \tag{2.6}$$

provided that (i) $dk_b \ll \mu$ (the corrugation slope μ is sub-critical, c.f. equation (2.8)), and (ii) $d\gamma \ll 1$ (i.e. the internal waves have a vertical wavelength $2\pi/\gamma$ much greater than the corrugation amplitude d).

Let us first consider the properties of the leading-order problem (i.e. eigenmodes and dispersion relation), by assuming a propagating wave solution of the form $w^{(1)} = W(z)e^{i(\mathbf{k}\cdot\mathbf{x}-\omega t)}$, where $\mathbf{k} = (k_x, k_y)$ is the horizontal wavenumber ($k = |\mathbf{k}|$) and ω is the frequency. Upon substitution in (2.2) with $b = 0$ we obtain the general Sturm-Liouville eigenvalue problem (e.g. *Thorpe*, 1966)

$$\left[(\omega^2 - f^2)d_z^2 + (N^2(z) - \omega^2)k^2\right]W(z) = 0, \ -h \leq z \leq 0, \tag{2.7a}$$

$$\left[(\omega^2 - f^2)d_z - gk^2\right]W(z) = 0, \ z = 0, \tag{2.7b}$$

$$W(z) = 0, \ z = -h, \tag{2.7c}$$

which can be solved analytically in terms of elementary (e.g. trigonometric, hyperbolic) or special functions (e.g. Airy, Bessel) for special density profiles $N(z)$, or numerically as a boundary value problem.

For a linearly varying mean density profile, i.e. such that $\bar{\rho}(z) = \rho_0(1 - az)$ (c.f. e.g. *Martin et al.*, 1972), the Brunt-Väisälä frequency is $N = \sqrt{ga} =$ constant. The vertical mode structure solution of (2.7) for $f < \omega < N$ becomes $W(z) = \sin\gamma(z + h)$ with $\gamma = k/\mu(\omega)$ the vertical wavenumber and

$$\mu(\omega) = \sqrt{\frac{\omega^2 - f^2}{N^2 - \omega^2}} \tag{2.8}$$

the internal wave slope. For $\omega < f$ or $N > \omega$ the solution reads $W(z) = \sinh\gamma(z + h)$ with $\gamma = k\sqrt{(\omega^2 - N^2)/(\omega^2 - f^2)}$. The dispersion relation is readily obtained in both cases upon substitution of $W(z)$ in (2.7b), i.e.

$$\mathcal{D}(\omega, k) \equiv 0, \text{ where } \begin{cases} \mathcal{D}(\omega, k) = \omega^2 - f^2 - \frac{gk^2}{\gamma}\tan\gamma h, \ f < \omega < N, \\ \mathcal{D}(\omega, k) = \omega^2 - f^2 - \frac{gk^2}{\gamma}\tanh\gamma h, \ \text{otherwise.} \end{cases} \tag{2.9}$$

The solutions (k, ω) to the dispersion relation (2.9) are three-dimensional surfaces in $(k_x h, k_y h, \omega/N)$ space, but since these surfaces are axisymmetric with respect to the ω/N axis we show them in figure 1 as two-dimensional curves in $(\omega/N, kh)$ space. We fix the stratification parameter as $ha = 0.01$, which corresponds to a 1% relative density increase between the free-surface and the bottom, and the Coriolis parameter is chosen as $f/N = 0.025$. For $\omega < f$, the only solutions are Poincaré waves that decay exponentially in one horizontal dimension (*Gill*, 1982), and we do not consider them. For $\omega \geq N$ only one solution k_0 exists in the first quadrant (with its mirrors in the other quadrants), whose associated fluid particle motion is maximum near the free surface and decreases as the depth increases ($\gamma_0 \in i\mathbb{R}$). Therefore this is basically a *surface* wave which is a little perturbed because of stratification. For $f < \omega < N$ there is an infinite number of solutions k_j ($j \in \mathbb{N}$) to (2.9). The first member of this set (k_0) is the continuation of the surface wave branch (shown close to the y axis in figure 1). All other waves ($k_j, j = 1, 2, \cdots$) have a sinusoidal vertical mode structure ($\gamma_j \in \mathbb{R}$) with fluid particle motions minimum near the free surface and seabed, and therefore these branches show *internal* waves.

2.2. **Chain resonance conditions.** The quadratic interaction term on the right-hand-side of (2.6) between an incident wave (wavenumber $\mathbf{k}$) and the bottom corrugations (wavenumber $\mathbf{k}_b$) indicates that the second-order velocity $w^{(2)}$ is forced by a term with wavenumber $\mathbf{k}^r = \mathbf{k} \pm \mathbf{k}_b$. Interestingly, the amplitude of the forced wave grows linearly in time unbounded when $\mathcal{D}(\omega, \mathbf{k}^r) = 0$ (c.f. equation (2.9)), i.e. when $\mathbf{k}^r$ is the wavenumber of a free wave (*Liu and Yue*, 1998). The condition that $\mathbf{k}^r$ satisfies the dispersion relation is known as the (wave-wave) resonance condition, or more specifically as the Bragg resonance condition in the case that one of the waves (here the bottom wave) is frozen (i.e. the amplitude is fixed, see *Davies* (1982)). When the resonance condition is satisfied, the perturbation expansion in (2.4) is not valid, and other methods (such as multiple scales) are necessary to obtain the growth rate of the resonant wave beyond the initial time. It is to be noted that *strong* energy exchanges can also be obtained when the resonance condition is only *nearly* satisfied, i.e. when $\mathcal{D}(\omega, \mathbf{k} \pm \mathbf{k}_b + \boldsymbol{\delta}) = 0$ with $\boldsymbol{\delta}/\boldsymbol{k_r} \ll 1$. Nearly resonant interactions, i.e. for which the detuning wavenumber $\boldsymbol{\delta} \neq \mathbf{0}$, will be shown to be of significant importance in the present analysis.

Contrary to in a homogeneous fluid, a single seabed harmonic $\mathbf{k}_b$ in a stratified fluid can resonate a large number of distinct triads, because the dispersion relation (2.9) admits an infinite number of wavenumber solutions. We can thus find two resonant triads $(\mathbf{k}_1, \mathbf{k}_2, \mathbf{k}_b)$ and $(\mathbf{k}_3, \mathbf{k}_4, \mathbf{k}_b)$, for different wavenumbers of the free waves. Importantly, different triads can exchange energy when they are *interconnected*, thus forming a resonance cluster, a concept used in turbulence wave theory (*L'vov et al.*, 2009; *Bustamante et al.*, 2014; *Tobisch*, 2016). Here, two triads resonated through the same bottom wavenumber $\mathbf{k}_b$ are interconnected when they share the same wavenumber of a free wave. An example of two such interconnected triads is shown in figure 2a: the wavenumber $\mathbf{k}_2$ is shared by both the lower and upper triad such that energy can be exchanged between the two triads through $\mathbf{k}_2$. Interestingly, larger resonance clusters can arise in a stratified fluid, i.e. including more than two triads (hence more than three waves), as described in the following section.

In a linearly-stratified fluid, the wavenumber (k_x, k_y) solutions of the dispersion relation can be represented by an infinite number of circles with radii k_j, as shown in figure 2b. For a given incident wavenumber $\mathbf{k}_{(0)}$ ($\vec{OI}$ in figure 2b) and bottom wavenumber $\mathbf{k}_b$, a series of forced waves is generated, owing to the successive

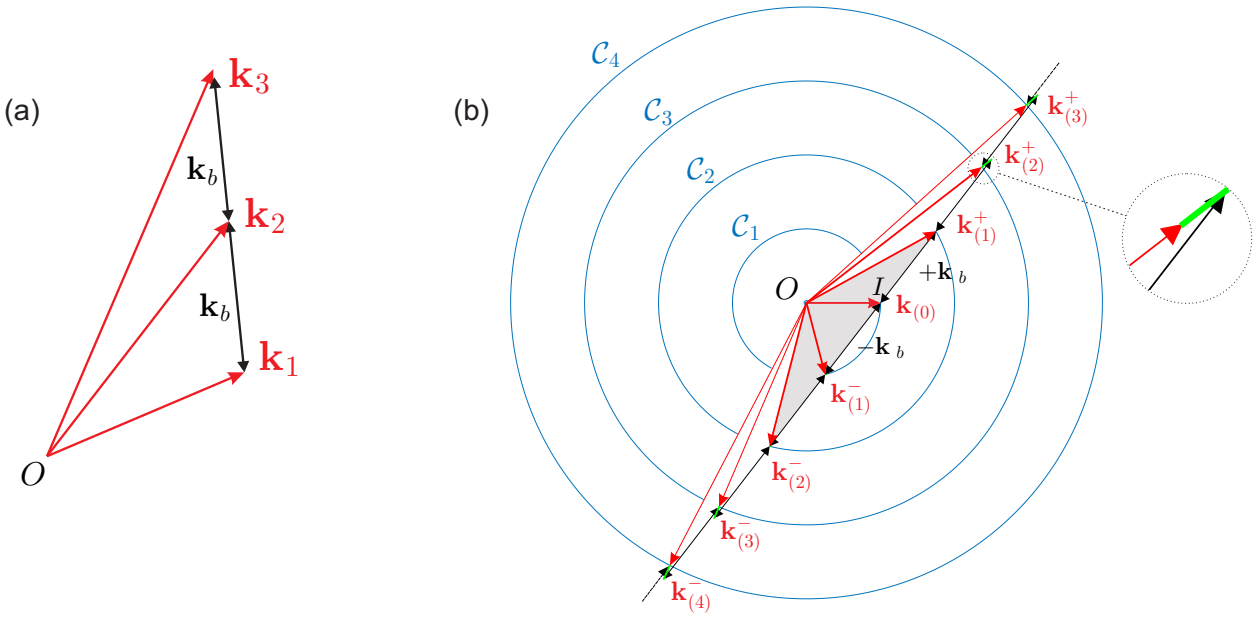

FIGURE 2. (a) Schematic representation of interconnected resonance. The wave $\mathbf{k}_1$, through the bottom component $\mathbf{k}_b$, generates (or resonates) wave $\mathbf{k}_2$. The resonant wave $\mathbf{k}_2$, through the same bottom component, generates $\mathbf{k}_3$. Energy can be modulated between the three waves. (b) In a linearly stratified ocean, associated with each frequency, there is an infinite number of natural wavenumbers, which can be represented by circles $\mathcal{C}_j$ of increasing radii k_j (c.f. equation (2.9)) with $j \in [0, \infty]$ (although note that $\mathcal{C}_0$ cannot be seen because the surface wavenumber is too small, i.e. $k_0 h \ll k_1 h$). An incident wave with wavenumber $\mathbf{k}_{(0)}$ interacting with a single bottom wavenumber $\mathbf{k}_b$, can therefore lead to a series of forced wavenumbers that are almost natural, hence resonant. The number of interconnected triads in this case grows as long as the sequentially forced wavenumbers $\mathbf{k}^{\pm}_{(m)} \pm \mathbf{k}_b$ are near-resonance. In this example, up to three interconnected triads (gray shaded) are perfectly resonant. All resonated waves in other triads experience some detuning (marked by overlaying thick solid lines), as can be best seen for $\mathbf{k}^+_{(2)}$ in the blow-up figure ($\boldsymbol{\delta}^+_2$ the detuning wavenumber).

quadratic wave-bottom interactions. The first forced waves have the wavenumbers $\mathbf{k}_{(0)} \pm \mathbf{k}_b$, which are perfectly resonant for the case shown in figure 2b, i.e. such that

$$\mathbf{k}_{(0)} \pm \mathbf{k}_b = \mathbf{k}^{\pm}_{(1)} \tag{2.10}$$

is the wavenumber of a free wave. The resonated waves with wavenumber $\mathbf{k}^{\pm}_{(1)}$ then also interact with the corrugations, forcing new waves with wavenumber $\mathbf{k}^{\pm}_{(1)} \pm \mathbf{k}_b$. In figure 2b, the forced wavenumber $\mathbf{k}^-_{(1)} - \mathbf{k}_b = \mathbf{k}^-_{(2)}$ is perfectly resonant but $\mathbf{k}^+_{(1)} + \mathbf{k}_b$ isn't. The detuning wavenumber between the forced wavenumber $\mathbf{k}^+_{(1)} + \mathbf{k}_b$ and the closest (in L_2-norm) wavenumber of a free wave $\mathbf{k}^+_{(2)}$ is non-zero, i.e. such that

$$\mathbf{k}^+_{(1)} + \mathbf{k}_b = \mathbf{k}^+_{(2)} - \boldsymbol{\delta}^+_2, \tag{2.11}$$

with $\boldsymbol{\delta}^+_2 \neq \mathbf{0}$ (c.f. blow-up in figure 2b). In figure 2b, the forced waves $(\mathbf{k}^+_{(1)}, \mathbf{k}^-_{(1)}, \mathbf{k}^-_{(2)})$ are perfectly resonant, and the $(\mathbf{k}^+_{(2)}, \mathbf{k}^+_{(3)}, \mathbf{k}^-_{(3)}, \mathbf{k}^-_{(4)})$ waves are near resonance. Near-resonance waves are important and considered in the present analysis because they can have a relatively large influence on the energy transfers between the perfectly tuned waves. Indeed, while the assumption that detuning weakens wave-wave interactions prevails, there are cases, as will be shown in §4.4, for which detuning can result in enhanced resonance (by order of magnitude).

For clarity of the formulation, let us briefly elaborate on the notations of the sequence of resonated wavenumbers, i.e.

$$\mathbf{k}^+_{(m-1)} + \mathbf{k}_b = \mathbf{k}^+_{(m)} - \boldsymbol{\delta}^+_m, \tag{2.12a}$$

$$\mathbf{k}^-_{(m-1)} - \mathbf{k}_b = \mathbf{k}^-_{(m)} - \boldsymbol{\delta}^-_m, \tag{2.12b}$$

for $m \geq 1$, with $\mathbf{k}^\pm_{(0)} = \mathbf{k}_{(0)}$ the incident wavenumber. The superscripts + (-) denote waves that are *positively* (*negatively*) generated, i.e. corresponding to what we call the *positive* (*negative*) branch of the chain resonance (2.12). The subscript m is the interaction number, i.e. such that e.g. $\mathbf{k}^-_{(2)}$ is the resonated wave obtained from the second series of wave-bottom interactions. It should be noted that the subscript m is put in between parenthesis because the m^{th} resonated wavenumber (with magnitude $k^\pm_{(m)}$) is not *a priori* an m^{th} wavenumber mode (i.e. $k^\pm_{(m)} \neq k_m$); for instance, in figure 2b, the $\mathbf{k}^+_{(1)}$ wave is a mode-two internal wave, not a mode one.

The resonated wavenumbers $\mathbf{k}^\pm_{(m)}$ are obtained such that the detuning $\|\boldsymbol{\delta}^\pm_m\|_2 = \delta^\pm_m$ is minimum (i.e. using the L^2-norm). As previously mentioned, the chain resonance can only include wavenumbers close to resonance, i.e. with small associated detuning. Here it is the cumulative detuning that needs to be small (as will be shown later), such that the condition for the $k^\pm_{(j)}$ wave to be part of the resonance cluster reads

$$\Delta^\pm_m = \frac{\delta^\pm_1 + \ldots + \delta^\pm_m}{k^\pm_{(m)}} \ll 1, \tag{2.13}$$

for all $m \leq j$. Note that the condition (2.13) implies that if the $\mathbf{k}^\pm_{(M^\pm)}$ wave is the first wave not included in the chain resonance, then neither are the $k^\pm_{(m)}$ waves ($m \geq M^\pm$).

3. Three-dimensional multiple-scale analysis

3.1. **Derivation of the envelope equations.** For bottom corrugations of small amplitudes, the evolution of the wave envelopes is slow compared to the variations of the carrier waves, such that we can use two different separated scales to describe the dynamics of the carrier waves and wave envelopes. The leading-order solution to the governing equation (2.2) can then be sought in the form

$$\begin{aligned} w^{(1)} = A_0(\bar{x},\bar{y},\bar{t})W_0(z)E_0(x,y,t) &+ \sum_{m=1}^{\infty} A^+_m(\bar{x},\bar{y},\bar{t})W^+_m(z)E^+_m(x,y,t) \\ &+ \sum_{m=1}^{\infty} A^-_m(\bar{x},\bar{y},\bar{t})W^-_m(z)E^-_m(x,y,t) + c.c., \end{aligned} \tag{3.1}$$

where A_0 and $A^\pm_m$ are the amplitudes of the the incident and resonated waves, which are functions of the slow variables $(\bar{x},\bar{y},\bar{t}) \sim \epsilon(x,y,t)$. The wavenumbers of the different waves involved in chain resonance are denoted by $\mathbf{k}^\pm_{(m)}$ (c.f. (2.12)), $W^\pm_m = \sin\gamma^\pm_{(m)}(z+h)$ is the vertical mode structure with $\gamma^\pm_{(m)} = k^\pm_{(m)}/\mu(\omega)$ (c.f. equation (2.8)), $E^\pm_m = \exp[i(\mathbf{k}^\pm_{(m)}\cdot\mathbf{x} - \omega t)]$, and *c.c.* denotes the complex conjugate. Denoting by $\theta^\pm_m$ the angle of the horizontal wavenumber $\mathbf{k}^\pm_{(m)}$ with the x axis, we then find from the momentum and continuity equations (2.7a)-(2.7b), using straightforward algebra, that

$$\begin{aligned} u^{(1)} =& A_0\partial_z W_0 \frac{iE_0\cos\theta_0}{k_{(0)}}(1 + i\frac{f}{\omega}\tan\theta_0) + \sum_{m=1}^{\infty} A^+_m\partial_z W^+_m \frac{iE^+_m\cos\theta^+_m}{k^\pm_{(m)}}(1 + i\frac{f}{\omega}\tan\theta^+_m) \\ &+ \sum_{m=1}^{\infty} A^-_m\partial_z W^-_m \frac{iE^-_m\cos\theta^-_m}{k^-_{(m)}}(1 + i\frac{f}{\omega}\tan\theta^-_m) + c.c., \end{aligned} \tag{3.2a}$$

$$\begin{aligned} v^{(1)} =& A_0\partial_z W_0 \frac{iE_0\sin\theta_0}{k_{(0)}}(1 - i\frac{f}{\omega}\operatorname{cotan}\theta_0) + \sum_{m=1}^{\infty} A^+_m\partial_z W^+_m \frac{iE^+_m\sin\theta^+_m}{k^\pm_{(m)}}(1 - i\frac{f}{\omega}\operatorname{cotan}\theta^+_m) \\ &+ \sum_{m=1}^{\infty} A^-_m\partial_z W^-_m \frac{iE^-_m\sin\theta^-_m}{k^-_{(m)}}(1 - i\frac{f}{\omega}\operatorname{cotan}\theta^-_m) + c.c.. \end{aligned} \tag{3.2b}$$

The variations of the leading-order wave amplitudes $A_m^{\pm}$ as functions of the slow space and time variables can be obtained from the so-called solvability condition, which ensures that the second-order solution is bounded in time and space (*Mei*, 1985). The equations for the wave amplitudes $A_m^{\pm}$ is thus derived upon inspection of the second-order problem for $w^{(2)}$ (i.e. (2.2a)-(2.2b) and (2.6)), which, with the consideration of the bottom corrugations and slow variations of the leading-order solution $w^{(1)}$, reads

$$[(\partial_t^2+f^2)\nabla^2+(N^2-f^2)\nabla_H^2]w^{(2)}=-2\partial_t\nabla^2\partial_{\bar{t}}w^{(1)}$$

$$-\partial_t^2(\nabla\cdot\bar{\nabla}+\bar{\nabla}\cdot\nabla)w^{(1)}-N^2(\nabla_H\cdot\bar{\nabla}_H+\bar{\nabla}_H\cdot\nabla_H)w^{(1)},\ -h\le z\le 0 \tag{3.3a}$$

$$[(\partial_t^2+f^2)\partial_z-g\nabla_H^2]w^{(2)}=-2\partial_t\partial_z\partial_{\bar{t}}w^{(1)},+g(\nabla_H\cdot\bar{\nabla}_H+\bar{\nabla}_H\cdot\nabla_H)w^{(1)},\ z=0, \tag{3.3b}$$

$$\epsilon w^{(2)}=u^{(1)}\partial_x b+v^{(1)}\partial_y b-b\partial_z w^{(1)},\ z=-h. \tag{3.3c}$$

Let us seek a second-order solution of the form

$$w^{(2)}=B_0(z)E_0+\sum_{m=1}^{\infty}B_m^{+}(z)E_m^{+}+\sum_{m=1}^{\infty}B_m^{-}(z)E_m^{-}+\textit{non-resonant terms}+\textit{c.c.} \tag{3.4}$$

where *non-resonant terms* denotes second-order terms that are not resonant, hence that do not affect the leading-order solution. Due to the fact that (3.3) is linear with respect to the flow variables, an equation can be obtained for each eigenmode $E_m^{\pm}$ independently, upon substitution from (3.4), (3.1), (3.2a), and (3.2b) for $w^{(2)}$, $w^{(1)}$, $u^{(1)}$ and $v^{(1)}$. The right-hand-side of equation (3.3c) is proportional to mode $E_m^{\pm}$ (i.e. with resonance wavenumber $\mathbf{k}_{(m)}^{\pm}$) when $\mathbf{k}_b$ interacts with wavenumber $\mathbf{k}_{(m-1)}^{\pm}$ or $\mathbf{k}_{(m+1)}^{\pm}$ (c.f. equations (2.12)). After standard algebraic manipulations, the equation for mode $E_m^{\pm}$ is thus obtained as

$$\left[\partial_z^2+(\gamma_{(m)}^{\pm})^2\right]B_m^{\pm}=2iW_m^{\pm}\frac{(k_{(m)}^{\pm})^2+(\gamma_{(m)}^{\pm})^2}{\omega^2-f^2}\omega\partial_{\bar{t}}A_m^{\pm}$$

$$+\frac{2i}{\mu^2}W_m^{\pm}\left[\mathbf{k}_{(m)}^{\pm}\cdot\bar{\nabla}_H A_m^{\pm}+(A_m^{\pm}/2)\bar{\nabla}_H\cdot\mathbf{k}_{(m)}^{\pm}\right],\ -h\le z\le 0, \tag{3.5a}$$

$$(\partial_z-\frac{\gamma_{(m)}^{\pm}}{\tan\gamma_{(m)}^{\pm}h})B_m^{\pm}=-2i\frac{\omega\gamma_{(m)}^{\pm}}{\omega^2-f^2}\cos\gamma_{(m)}^{\pm}h\partial_{\bar{t}}A_m^{\pm}$$

$$-2i\frac{g}{\omega^2-f^2}\sin\gamma_{(m)}^{\pm}h\left[\mathbf{k}_{(m)}^{\pm}\cdot\bar{\nabla}_H A_m^{\pm}+(A_m^{\pm}/2)\bar{\nabla}_H\cdot\mathbf{k}_{(m)}^{\pm}\right],\ z=0, \tag{3.5b}$$

$$\epsilon B_m^{\pm}=-\frac{D\gamma_{(m)}^{\pm}}{2}\left[A_{m-1}^{\pm}\mathcal{P}_{m-1}^{\pm}e^{\pm i\varphi_b}e^{-i\boldsymbol{\delta}_m^{\pm}\cdot\boldsymbol{x}}+A_{m+1}^{\pm}\mathcal{N}_{m+1}^{\pm}e^{\mp i\varphi_b}e^{i\boldsymbol{\delta}_{j(m+1)}^{\pm}\cdot\boldsymbol{x}}\right],\ z=-h, \tag{3.5c}$$

where

$$\mathcal{P}_{m-1}^{\pm}=\frac{1}{k_{(m)}^{\pm}k_{(m-1)}^{\pm}}\left[\mathbf{k}_{(m)}^{\pm}\cdot\mathbf{k}_{(m-1)}^{\pm}+i\frac{f}{\omega}\mathbf{k}_{(m)}^{\pm}\times\mathbf{k}_{(m-1)}^{\pm}\right]+\mathcal{O}(\delta_m^{\pm}/k_{(m)}^{\pm}), \tag{3.6a}$$

$$\mathcal{N}_{m+1}^{\pm}=\frac{1}{k_{(m)}^{\pm}k_{(m+1)}^{\pm}}\left[\mathbf{k}_{(m)}^{\pm}\cdot\mathbf{k}_{(m+1)}^{\pm}+i\frac{f}{\omega}\mathbf{k}_{(m)}^{\pm}\times\mathbf{k}_{(m+1)}^{\pm}\right]+\mathcal{O}(\delta_m^{\pm}/k_{(m)}^{\pm}). \tag{3.6b}$$

The inhomogeneous equation (3.5) for $B_m^{\pm}$ has a unique solution if and only if the forcing terms on the right-hand-side satisfy the solvability condition (*Fredholm*, 1903; *Nayfeh and Kandil*, 1978). The solvability condition is obtained by doing the integration in z as follows

$$\int_{z=-h}^{0}dz\left\{W_m^{\pm}[\partial_z^2+(\gamma_{(m)}^{\pm})^2]B_m^{\pm}-B_m^{\pm}(\partial_z^2+\gamma_j^2)W_m^{\pm}\right\}$$

$$=\int_{z=-h}^{0}dz\left\{W_m^{\pm}[\partial_z^2+(\gamma_{(m)}^{\pm})^2]B_m^{\pm}\right\}, \tag{3.7}$$

which, upon integration by parts, gives

$$[W_m^{\pm}\partial_z B_m^{\pm}]_{-h}^{0}-[B_m^{\pm}\partial_z W_m^{\pm}]_{-h}^{0}. \tag{3.8}$$

Substituting the boundary conditions (3.5b)-(3.5c) at $z = 0, -h$ for $B_m^{\pm}$ in (3.8), and directly integrating (3.7) using (3.5a), we then get after tedious but straightforward algebra the final equation

$$\begin{aligned} &\partial_t A_m^{\pm} + \mathbf{C}_{gm}^{\pm} \cdot \nabla_H A_m^{\pm} + \frac{A_m^{\pm}}{2} \nabla_H \cdot \mathbf{C}_{gm}^{\pm} = \\ &i\Omega_m^{\pm} \left[A_{m-1}^{\pm} \mathcal{P}_{m-1}^{\pm} e^{\pm i\varphi_b} e^{-i\boldsymbol{\delta}_m^{\pm} \cdot \boldsymbol{x}} + A_{m+1}^{\pm} \mathcal{N}_{m+1}^{\pm} e^{\mp i\varphi_b} e^{i\boldsymbol{\delta}_{m+1}^{\pm} \cdot \boldsymbol{x}} \right]. \end{aligned} \tag{3.9}$$

In (3.9), $\mathbf{C}_{gm}^{\pm} = \{C_{gmx}^{\pm}, C_{gmy}^{\pm}\}$ is the horizontal wave group speed such that

$$\mathbf{C}_{gm}^{\pm} = \left\{ \frac{\partial \omega}{\partial k_x}, \frac{\partial \omega}{\partial k_y} \right\} = \frac{\omega \mathbf{k}_{(m)}^{\pm}}{(k_{(m)}^{\pm})^2} \frac{(\omega^2 - f^2)}{\omega^2} \frac{2\gamma_{(m)}^{\pm} h + \sin 2\gamma_{(m)}^{\pm} h}{\left[(1-\mu^2) \sin 2\gamma_{(m)}^{\pm} h + (1+\mu^2) 2\gamma_{(m)}^{\pm} h \right]}, \tag{3.10}$$

and

$$\Omega_m^{\pm} = \omega \frac{d}{2h} \frac{(\omega^2 - f^2)}{\omega^2} \frac{2\gamma_{(m)}^{\pm} h}{\left[(1-\mu^2) \sin 2\gamma_{(m)}^{\pm} h + (1+\mu^2) 2\gamma_{(m)}^{\pm} h \right]} \tag{3.11}$$

is a characteristic slow frequency. Note that equation (3.9) applies for each of the *positively* A_m^+ and *negatively* A_m^- resonated waves independently. A similar equation is also obtained for the incident wave, i.e.

$$\partial_t A_0 + \mathbf{C}_{g0} \cdot \nabla_H A_0 + \frac{A_0}{2} \nabla_H \cdot \mathbf{C}_{g0} = i\Omega_0 \left[A_1^- \mathcal{N}_1^- e^{i\varphi_b} e^{i\boldsymbol{\delta}_1^- \cdot \boldsymbol{x}} + A_1^+ \mathcal{N}_1^+ e^{-i\varphi_b} e^{i\boldsymbol{\delta}_1^+ \cdot \boldsymbol{x}} \right]. \tag{3.12}$$

The coupled internal wave envelope equations (3.9) can be shown to be constrained by an energy-type preserving equation. Multiplying each equation in (3.9) and (3.12) by $(A_m^{\pm})^*/\Omega_m^{\pm}$ (where superscript $*$ denotes the complex conjugate), and summing them over m along with their complex conjugate we obtain

$$\left[\partial_t \left(\frac{|A_0|^2}{\Omega_0} \right) + \nabla_H \cdot \left(\mathbf{C}_{g0} \frac{|A_0|^2}{\Omega_0} \right) \right] + \sum_{m=1}^{\infty} \left[\partial_t \left(\frac{|A_m^{\pm}|^2}{\Omega_m^{\pm}} \right) + \nabla_H \cdot \left(\mathbf{C}_{gm}^{\pm} \frac{|A_m^{\pm}|^2}{\Omega_m^{\pm}} \right) \right] = 0. \tag{3.13}$$

For a problem spatially uniform, i.e. such that $\nabla_H \equiv \mathbf{0}$, equation (3.13) shows that the so-called total wave action $\mathcal{A} = \mathcal{A}_0 + \sum_{m=1}^{\infty} (\mathcal{A}_m^+ + \mathcal{A}_m^-)$ remains constant over time, where

$$\mathcal{A}_m^{\pm} = |A_m^{\pm}|^2 / \Omega_m^+. \tag{3.14}$$

For a problem that is not uniform in space but at the steady-state (i.e. $\partial_t \equiv 0$), on the other hand, it is the total energy flux $\mathbf{F} = \mathbf{F}_0 + \sum_{m=1}^{\infty} (\mathbf{F}_m^+ + \mathbf{F}_m^-)$ that is conserved, with

$$\mathbf{F}_m^{\pm} = \mathbf{C}_{gm}^{\pm} |A_m^{\pm}|^2 / \Omega_m^+. \tag{3.15}$$

The wave action $\mathcal{A}_m^{\pm}$ is proportional to the internal wave energy density $KE_m^{\pm} + PE_m^{\pm}$, where

$$\begin{aligned} KE_m^{\pm} &= \int d\mathbf{x} \int_{-h}^{0} dz \frac{\rho_0}{2} \left[(u_m^{\pm})^2 + (v_m^{\pm})^2 + (w_m^{\pm})^2 \right], \\ PE_m^{\pm} &= \int d\mathbf{x} \int_{-h}^{0} dz \frac{\rho_m'^{\pm 2} g^2}{2\rho_0 N^2} + \int d\mathbf{x} \int_{0}^{\eta_m^{\pm}} dz \rho_0 g z. \end{aligned}$$

It is important to note that the total wave action and energy flux are conserved quantities only because we assume that the normalized detuning terms are small, i.e. $\delta_m^{\pm}/k_{(m)}^{\pm} \ll 1$, such that they can be dropped from the expression for $\mathcal{P}_{m-1}^{\pm}$ and $\mathcal{N}_{m+1}^{\pm}$ in (3.6). This implies that forced waves with too large of a detuning cannot be included in the multiple-scale solution, as will be further discussed in §3.2.

It should be noted that $\bar{\nabla}$ and ∇ in (3.3a)-(3.3b) do not commute because we allow the mean waterdepth to be a slowly varying function of the horizontal variables, i.e. $h = h(\bar{x}, \bar{y})$. Interestingly, we also note that two waves that are perpendicular, i.e. such that $\mathbf{k}_{(m)} \cdot \mathbf{k}_{(m+1)}^{\pm} = 0$, cannot exchange energy when the Coriolis effect is neglected ($f = 0$), since the coupling coefficients $\mathcal{P}_{m-1}^{\pm}$ or $\mathcal{N}_m^{\pm}$ become zero in this case (c.f. equation (3.6)). This phenomenon is known as Bragg degenerate resonance in homogeneous water and is shown to hold here for a stratified fluid without rotation (*Couston et al.*, 2016). For completeness, we shall finally

point out that (3.9) also applies under rigid-lid assumption upon consideration of the group velocities and (unique) coupling slow frequency

$$\mathbf{C}_{gm}^{\pm,rig} = \frac{\omega \mathbf{k}_{(m)}^{\pm,rig}}{(k_{(m)}^{\pm,rig})^2} \frac{(\omega^2 - f^2)}{\omega^2(1+\mu^2)},\ \Omega^{c,rig} = \omega \frac{d}{2h} \frac{(\omega^2 - f^2)}{\omega^2(1+\mu^2)}, \tag{3.17}$$

where the wavenumber $k_{(m)}^{\pm,rig} = \|\mathbf{k}_{(m)}^{\pm,rig}\|_2$ is given by the dispersion relation

$$(k_{(m)}^{\pm,rig})^2 = \left[\frac{(m)\pi}{h}\right]^2 \frac{\omega^2 - f^2}{N^2 - \omega^2}, \tag{3.18}$$

with (m) the (integer) mode number of the resonated wave.

3.2. **Solution method at the steady state.** Here we consider constant mean waterdepth h, i.e. such that the term $\nabla_H \cdot \mathbf{C}_{gm}^{\pm}$ in (3.9) can be dropped, and we take sinusoidal corrugations for which $\varphi_b = -\pi/2$ (c.f. (2.3)). Using the scaled amplitude variables $A_m^{\pm} = \bar{A}_m^{\pm} \exp(-i\boldsymbol{\Delta}_m^{\pm} \cdot \mathbf{x})$ where

$$\boldsymbol{\Delta}_m^{\pm} = \boldsymbol{\delta}_1^{\pm} + ... + \boldsymbol{\delta}_m^{\pm} \tag{3.19}$$

is the cumulative detuning wavenumber, the envelope equations (3.9) can then be rewritten as

$$\left(\partial_t + \mathbf{C}_{gm}^{\pm} \cdot \nabla_H\right) \bar{A}_m^{\pm} - i \left(\mathbf{C}_{gm}^{\pm} \cdot \boldsymbol{\Delta}_m^{\pm}\right) \bar{A}_m^{\pm} = \Omega_m^{\pm} \left(\pm \bar{A}_{m-1}^{\pm} \mathcal{P}_{m-1}^{\pm} \mp \bar{A}_{m+1}^{\pm} \mathcal{N}_{m+1}^{\pm}\right), \tag{3.20}$$

where the additional term on the left-hand-side comes from the re-scaling of the amplitude variables and is due to the fact that some of the interactions are not perfectly resonant.

The system of envelope equations (3.20) has constant coefficients and is amenable to simple analytical treatment using an eigenmode decomposition. For a patch of corrugations of finite extent in x but infinitely long in y, the steady-state problem is independent of both y and t such that the solution

$$\left\{\bar{A}_m^{\pm}\right\} = (...\bar{A}_m^{-}, ...\bar{A}_1^{-}, \bar{A}_0, \bar{A}_1^{+}, ...\bar{A}_m^{+}, ...), \tag{3.21}$$

written in vector form, is to be found as a solution of the matrix equation

$$\partial_x \left\{\bar{A}_m^{\pm}\right\} = [E]\left([S] + i[F] + i[D]\right)\left\{\bar{A}_m^{\pm}\right\}. \tag{3.22}$$

The matrix $[E]$, $[D]$, $[S]$ and $[F]$ are real and given by

$$[E] = \begin{bmatrix} \ddots & & & & \\ & \frac{\Omega_1^-}{C_{g1x}^-} & & (0) & \\ & & \frac{\Omega_0}{C_{g0x}} & & \\ & (0) & & \frac{\Omega_1^+}{C_{g1x}^+} & \\ & & & & \ddots \end{bmatrix},\ [D] = \begin{bmatrix} \ddots & & & & \\ & \frac{\mathbf{C}_{g1}^- \cdot \boldsymbol{\Delta}_1^-}{\Omega_1^-} & & (0) & \\ & & 0 & & \\ & (0) & & \frac{\mathbf{C}_{g1}^+ \cdot \boldsymbol{\Delta}_1^+}{\Omega_1^+} & \\ & & & & \ddots \end{bmatrix},$$

with $[S] + i[F]$ a skew-Hermitian matrix written as

$$\begin{bmatrix} \ddots & \ddots & \ddots & & & & & & & \\ & \mathcal{N}_{m+1}^- & 0 & -\mathcal{P}_{m-1}^- & & & & (0) & & \\ & & \ddots & \ddots & \ddots & & & & & \\ & & & \mathcal{N}_2^- & 0 & -\mathcal{P}_0^- & & & & \\ & & & & \mathcal{N}_1^- & 0 & -\mathcal{N}_1^+ & & & \\ & & & & & \mathcal{P}_0^+ & 0 & -\mathcal{N}_2^+ & & \\ & & & & & & \ddots & \ddots & \ddots & \\ & & & (0) & & & & \mathcal{P}_{m-1}^+ & 0 & -\mathcal{N}_{m+1}^+ \\ & & & & & & & & \ddots & \ddots & \ddots \end{bmatrix}.$$

In practice the infinite system of equations is truncated to a finite number of *positively* (M^+) and *negatively* resonated wave modes (M^-), such that we can instead solve the truncated system

$$\partial_x \left\{\bar{A}_m^{\pm}\right\}^N = [E]^N \left([S]^N + i[F]^N + i[D]^N\right)\left\{\bar{A}_m^{\pm}\right\}^N. \tag{3.23}$$

The matrices and vectors with superscripts N have finite size, such that e.g. $\left\{\bar{A}_m^{\pm}\right\}^N = (\bar{A}_{M^-}^-, ...\bar{A}_1^-, \bar{A}_0, \bar{A}_1^+, ...\bar{A}_{M^+}^+)$ has been truncated to $N = M^+ + M^- + 1$ degrees of freedom. The truncation arises as a simplification of the solution because (i) a finite patch cannot resonate waves with infinite wavenumbers (the chain resonance being sequential), and (ii) waves far from resonance do not capture much energy and therefore do not contribute significantly to the system's dynamics. The choice of M^+ and M^- thus must satisfy two types of requirements, that are: (i) waves with large normalized cumulative detuning are discarded, i.e. for which $\Delta_m^{\pm}/k_{(m)}^{\pm} > \tau$, where $\tau \ll 1$ is a small threshold parameter (here we will use $\tau = 10\%$), and (ii) a large enough number of near-resonance waves is considered such that the solution is converged. Importantly, the first condition also ensures that a separation of scales truly exists between the variations of the carrier waves and wave envelopes, such that the multiple-scale results remain valid at leading order. Here the cumulative detuning $\mathbf{\Delta}_m^{\pm}$ is the most informative measure of detuning because it is $\mathbf{\Delta}_m^{\pm}$ that appears in matrix $[D]^N$ in the system of equations (3.23). It is for this reason that the chain resonance condition (2.13) involves $\Delta_m^{\pm}$, rather than $\delta_m^{\pm}$.

The solution to the matrix equation (3.23) is sought as a superposition of eigenmodes, i.e. such that

$$\left\{\bar{A}_m^{\pm}\right\}^N = \sum_{i=0}^{N} c_i \left\{a\right\}_i^N e^{\alpha_i x/\lambda_1}, \tag{3.24}$$

where $\lambda_1 = 2\pi/k_1$ is the wavelength of the incident wave. The eigenvectors $\left\{a_j\right\}_i^N$ are found by solving the eigenvalue problem

$$\alpha_i \left\{a\right\}_i^N = \lambda_1 [E]^N \left([S]^N + i[F]^N + i[D]^N\right) \left\{a\right\}_i^N, \tag{3.25}$$

while the coefficients c_i are obtained from enforcing the boundary conditions. The boundary conditions are applied at the beginning of the patch ($x = 0$) for waves that are transmitted, i.e. such that $\mathbf{C}_{gm}^{\pm} \cdot \hat{x} > 0$, and at the end of the patch ($x = l$) for waves that are reflected, i.e. such that $\mathbf{C}_{gm}^{\pm} \cdot \hat{x} < 0$.

The presence of reflected waves can have a significant effect on the system dynamics. Indeed, with only transmitted waves, the eigenvalues α_i of (3.25) are all pure imaginary because the system's matrix is the product of $([S]^N + i[F]^N + i[D]^N)$, which is a skew-Hermitian matrix (because $\mathcal{P}_{m-1}^{\pm} = (\mathcal{N}_m^{\pm})^*$, see equation (3.6)), with $[E]$, which is a positive definite matrix. The solution behavior is therefore oscillatory as can be expected for waves propagating in the same direction. With reflected waves, however, $[E]$ is not positive definite such that the eigenvalues, or at least some of them, have a non zero real part. This is in agreement with a net decaying behavior of some of the incident and transmitted waves to the downstream of the patch, versus a net growing behavior to the upstream for the reflected waves.

4. Results and discussion

We solve in this section the boundary-value problem (3.23) as a function of the corrugation angle θ_b (c.f. equation (2.3)), for a patch of finite extent in the x direction starting at $x = 0$. The corrugation wavenumber is of the same order as the mode-one internal wave wavenumber, i.e. $k_b/k_1 \sim \mathcal{O}(1)$, and is taken such that the incident wave and bottom corrugations perfectly resonate the $\mathbf{k}_{(1)}^+$ wave (see figure 2b). We focus our attention on incident waves propagating in $+x$ direction that are mode-one internal waves. This is motivated by the fact that most of the internal wave energy is stored in low mode number waves (*Garrett and Munk*, 1979), and because such long waves can propagate over long distances and interact with topographies (*St Laurent and Garrett*, 2002; *Zhao et al.*, 2010). The number of seabed corrugations is chosen in order to highlight the different physics of chain resonance, hence varies depending on the different cases investigated, but we keep it to a minimum (i.e. few tens of corrugations) such that the results may be applicable for practical situations. Our analysis in §4.1-§4.4 assumes constant physical parameters ha, ω/N and f/N, and considers that there are no reflective boundaries, i.e. such that internal waves leaving the corrugated patch are radiated away. In §4.5, the analysis is generalized as we discuss how the results are affected by changing these physical parameters.

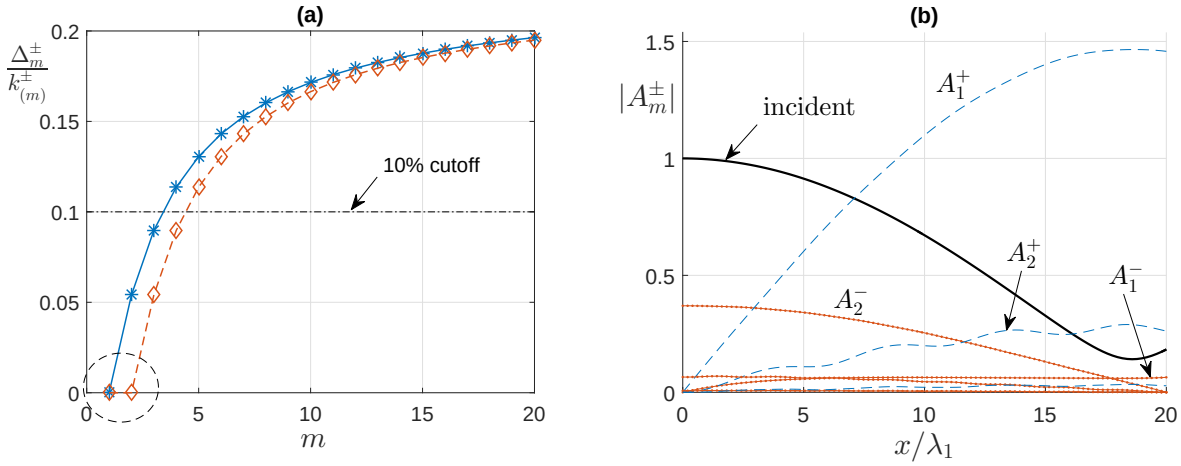

FIGURE 3. (a) Detuning $\Delta_m^\pm/k_{(m)}^\pm$ of the successively resonated waves A_m^+ (solid line) and A_m^- (dash-dotted line) as a function of the interaction number m. The bottom wavenumber and angles are given by equation (4.1), i.e. such that A_1^+, A_1^- and A_2^- have zero detuning (highlighted in dashed circle). Eight waves are considered in the chain resonance with a 10% cutoff detuning. (b) Evolution of the envelope amplitudes of the resonated waves as predicted by equation (3.23) (with $M^+ = 3$, $M^- = 4$) for a patch of length $l = 20\lambda_1$. The chain resonance results in significant energy transfers from the incident to the transmitted A_1^+ and A_2^+ waves, as well as to the reflected wave A_2^- (marked as 2^-). The physical parameters are $d/h = 0.02$, $f/N = 0.025$, $N^2 g/h = ha = 0.01$ and $\omega/N = 0.1$.

4.1. **Oblique chain resonance with three perfect resonances.** Let us first present a case study of oblique chain resonance with corrugation wavenumber k_b and angle θ_b selected such that

$$\theta_b = \theta_b^* = \arccos\left(\sqrt{\frac{k_2^2 - k_1^2}{8k_1^2}}\right), \quad k_b = 2k_1 \cos\theta_b, \tag{4.1}$$

which is the case shown in figure 2b. The three generated waves $\mathbf{k}_{(1)}^+$, $\mathbf{k}_{(1)}^-$ and $\mathbf{k}_{(2)}^-$ are perfectly resonant and have zero detuning, i.e. $\delta_1^+ = \delta_1^- = \delta_2^- = 0$ (highlighted by a dashed circle in figure 3a). Other successively generated waves experience some detuning (e.g. $\mathbf{k}_{(2)}^+$, see figure 2b), which increases with the interaction number m, as shown in figure 3a. As discussed §3.2 (c.f. equation (3.23)), here we limit the multiple-scale analysis to resonant waves with less than 10% detuning. As a result, we consider eight resonant waves in the chain resonance (c.f. figure 3a).

We show in figure 3b the evolution of the wave amplitudes $|A_m^\pm|$ over the corrugated patch (corrugations in $0 \le x/\lambda_1 \le 20$), with bottom amplitude $d/h = 0.02$. We solve equation (3.23) with boundary conditions enforced at $x = 0$ for the incident and transmitted waves, i.e. such that $A_0 = 1$, $A_m^+ = 0$ ($m = 1, 2, 3$), and $A_1^- = 0$, and at $x = l$ (i.e. the end of the patch) for the reflected waves, i.e. such that $A_m^- = 0$ for $m = 2, 3, 4$. An example of reflected wave can be clearly seen in figure 3b as the wave A_2^- grows from the downstream toward the beginning of the patch. The wave A_1^-, on the other hand, is transmitted, i.e. it propagates in the $+x$ direction, and thus shows a different behavior. This is a three-dimensional effect, since with $\theta_b = 0$ A_1^- would be necessarily reflected. The exchanges of energy are dominated by the interaction of the pair of A_0 and A_1^+ waves, which propagate in the same $+x$ direction. The variations of the wave amplitudes are mostly modulated (i.e. oscillatory), such that the incident wave amplitude would grow again for a longer patch (not shown). An estimate for the maximum of A_1^+ over the patch can be obtained from the conservation of wave action (3.13), which, assuming $\partial_t \equiv \partial_y \equiv 0$, reduces to

$$\hat{x} \cdot \left[\mathbf{F}_0 + \sum_{m=1}^{M^+} \mathbf{F}_m^+ + \sum_{m=1}^{M^-} \mathbf{F}_m^-\right] = \hat{x} \cdot \mathbf{F}_0(x = 0), \tag{4.2}$$

i.e. the energy flux in x direction is conserved (c.f. equation (3.15)). Neglecting waves other than A_0 and A_1^+ and assuming that $A_0 = 0$ when A_1^+ is maximum, equation (4.2) then yields

$$\max_x |A_1| = \sqrt{\frac{\Omega_1^+ C_{g0x}}{\Omega_0 C_{g1x}^+}}. \tag{4.3}$$

For the physical parameters of figure 3b, (4.3) gives $\max_x |A_1| \sim 1.51$, i.e. a value slightly larger than the actual maximum reached by A_1^+ (i.e. 1.47).

From figure 3b, we see that the A_2^+ wave grows up to about 25% of the incident wave amplitude over the corrugated patch, while detuned by more than 5%. Detunings on the order of a few percents thus do not always prevent waves from growing relatively large, which demonstrates that near-resonance waves cannot be always neglected. The evolution of the wave amplitudes A_0, A_m^+ ($m = 1, 2, 3$), and A_m^- ($m = 1, 2, 3, 4$) as shown in figure 3b, however, does not change substantially when including more waves in the chain resonance, i.e. waves with detuning greater than 10%. Solving equation (3.23) for 10 *positively* and *negatively* forced waves (i.e. $M^+ = M^- = 10$ such that the largest detuning is about 17%), for instance, we find that the variations of the incident wave differ by only 0.01% from what we obtained with $M^+ = 3$ and $M^- = 4$ (shown in figure 3b). This suggests that waves with relatively large detuning (but still small) do not affect the system dynamics, such that the 10% threshold ensures the validity of the multiple-scale assumption without impacting the solution accuracy.

4.2. **Chain resonance at all corrugation angles.** In order to assess whether a chain resonance as shown in §4.1 can occur for other relative angles between the incident wave and the seabed undulations, we must first check that the detuning of the successively forced waves remains small as the orientation of the seabed bars changes from being parallel to being perpendicular with respect to the incident waves $\mathbf{k}_{(0)}$ (see figure 2b). We restrict our analysis to the case where the first wave A_1^+ is perfectly resonant, i.e. we select $\mathbf{k}_b$ such that $\mathbf{k}_{(0)} + \mathbf{k}_b = \mathbf{k}_{(1)}^+$ with $\mathbf{k}_{(1)}^+$ the wavenumber of a free wave. Therefore, the corrugation wavenumber changes when the bottom angle is varied.

We show in figure 4 the normalized detuning $\Delta_m^\pm / k_{(m)}^\pm$ of the first ten resonated waves ($m = 1, ..10$, c.f. equation (2.13)), as a function of the corrugation angle $\theta_b \in [0,\ \pi/2]$, with $k_{(1)}^+ = k_2$. The upper half of the plot shows the detuning of the $\mathbf{k}_{(m)}^+$ waves (i.e. the *positive* branch of the chain resonance, c.f. (2.12a)), while the lower plot shows the detuning of the $\mathbf{k}_{(m)}^-$ waves (the *negative* branch, c.f. (2.12b)). The long thick black line running along the x axis of the upper plot shows the detuning wavenumber for the $k_{(1)}^+$ waves (which is $\Delta_1^+ = \delta_1^+ = 0$ by construction), and has been colored in black for clarity. The detuning of other quasi-perfect resonant waves, i.e. with $\Delta_m^\pm / k_{(m)}^\pm < 0.01\%$, has also been colored in black, as can be seen for small θ_b (highlighted by the arrow i in figure 4). White regions of the figure show waves that are not considered in a chain resonance due to detuning $\Delta_m^\pm / k_{(m)}^\pm$ exceeding the 10% threshold, which was decided based on the fact that this threshold satisfies the multiple-scale assumption while retaining a good solution accuracy (see §4.1).

The special case of two-dimensional problem with a rigid-lid assumption is known to lead to a perfect chain resonance that is also called geometric focusing (see *Bühler and Holmes-Cerfon*, 2011; *Karimpour et al.*, 2016). Here, we obtain the perfect chain resonance counterpart with free surface for a small oblique incidence (i.e. $\theta_b \sim 0.05$, see i in figure 4), due to the fact that the spacing between two successive internal wave wavenumbers decreases with the mode number. Importantly, the detuning $\Delta_m^+ / k_{(m)}^\pm$ is small for almost all θ_b, such that the occurrence of chain resonance (i.e. with a number $N \geq 2$ of generated waves) is not limited to quasi co-directional waves and corrugations crests. For θ_b as large as $\pi/8$, for instance, we find that $\Delta_{10}^+ \sim 3\%$, such that at least 10 different internal waves enter the chain resonance.

The *negatively* generated waves $k_{(1)}^-$ have detuning $\Delta_1^- / k_{(1)}^- > 10\%$ for almost all θ_b, as shown by the predominantly white lower half of figure 4, such that they are typically neglected from the chain resonance. For $\theta_b \lesssim \pi/4$, there is a narrow range of corrugation angles that results in small enough detuning, i.e. $\Delta_1^- / k_{(1)}^- < 10\%$ (c.f. ii in figure 4), due to the fact that the forced wavenumber $k_{(0)} - \mathbf{k}_b$ is close to the surface-wave wavenumber k_0. The surface wave does not yet capture a significant fraction of the incident wave energy in this case (i.e. ii in figure 4) because $\mathbf{k}_{(1)}^-$ is perpendicular to $\mathbf{k}_{(0)}$, such that the coupling coefficient is 0 between the two waves (c.f. equation (3.9)). For θ_b greater but close to $\pi/4$, however, the

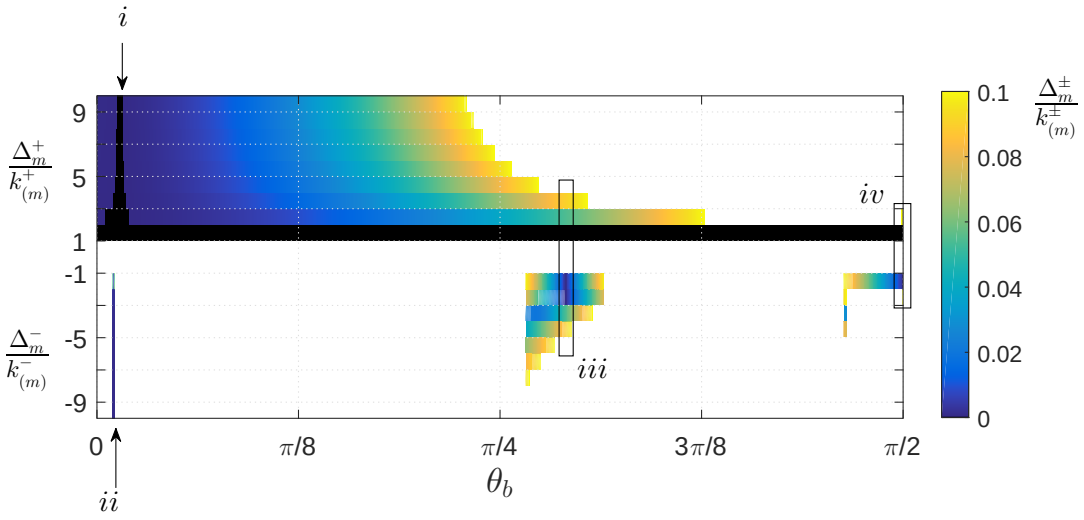

FIGURE 4. Normalized detuning wavenumber $\Delta^+_m/k^+_{(m)}$ (upper half of the plot) and $\Delta^-_m/k^-_{(m)}$ (lower half) given by equation (2.13), shown for the first 10 resonated waves (y axis) as a function of the corrugation angle θ_b (x axis). The color scheme indicates the strength of detuning, which is shown in black when $\Delta^\pm_m/k^\pm_{(m)} < 0.01\%$ (perfect or almost perfect resonance). The detuning for waves $\Delta^\pm_m/k^\pm_{(m)}$ in a chain resonance experiencing large detuning, i.e. for which $\exists j$ such that $\Delta^\pm_j/k^\pm_{(j)} > 10\%$, has been whited out for all $m \geq j$. Large resonance clusters are obtained for a broad range of angles when keeping waves with up to 10% detuning. The roman numerals highlight some of the key chain resonance that are further discussed in the text. The bottom wavenumber k_b is chosen such that $k^+_{(1)} = k_2$, and the other physical parameters are the same as those of figure 3.

detuning $\Delta^-_1/k^-_{(1)}$ decreases significantly because the forced wavenumber $k_{(0)} - \mathbf{k}_b$ is close to the mode-one internal wavenumber, i.e. $\|k_{(0)} - \mathbf{k}_b\|_2 \sim k_1$. The chain resonance marked by *iii* in figure 4 is such an example of chain resonance including *negatively* generated waves $k^-_{(m)}$, which is in fact the case investigated in 4.1. The detuning $\Delta^-_1/k^-_{(1)} < 10\%$ becomes also relatively small as $\theta_b \to \pi/2$, i.e. when the corrugation crests are perpendicular to the incident waves (*iv* in figure 4).

Similar plots for the detuning are shown in figure 5a-b for shorter bottom corrugations, i.e. such that $k^+_{(1)} = k_3$ and $k^+_{(1)} = k_4$ (compared to $k^+_{(1)} = k_2$ in figure 4). The successively resonated waves have higher wavenumbers, and result in overall in smaller normalized detuning wavenumbers $\Delta^\pm_m/k^\pm_{(m)}$. For $\theta_b \sim 0$, this is due to the fact that the forced wavenumber $\mathbf{k}_{(0)} - \mathbf{k}_b \sim (k_1 - k_b)\hat{x} \sim -k_1\hat{x}$ in figure 5a, which is the wavenumber of a mode-one internal wave propagating in the $-x$ direction (i.e. reflected), hence resonant. For figure 5b, we have instead $\mathbf{k}_{(0)} - \mathbf{k}_b \sim (k_1 - k_b)\hat{x} \sim -k_2\hat{x}$, which is the wavenumber of a reflected mode-two internal wave, hence again resonant.

4.3. **Spatial dynamics of chain resonance.** The analysis of the occurrence of chain resonance of figure 4-5 indicates how many waves are forced when the incident wave propagates over the corrugations, but not how strongly they interact with each other. Consequently, in this section we elaborate on the dynamics of chain resonance for the two extreme cases of oblique chain resonance, i.e. when $\theta_b \sim 0$ is small (figure 6) and when $\theta_b = \pi/2$ is large (figure 7).

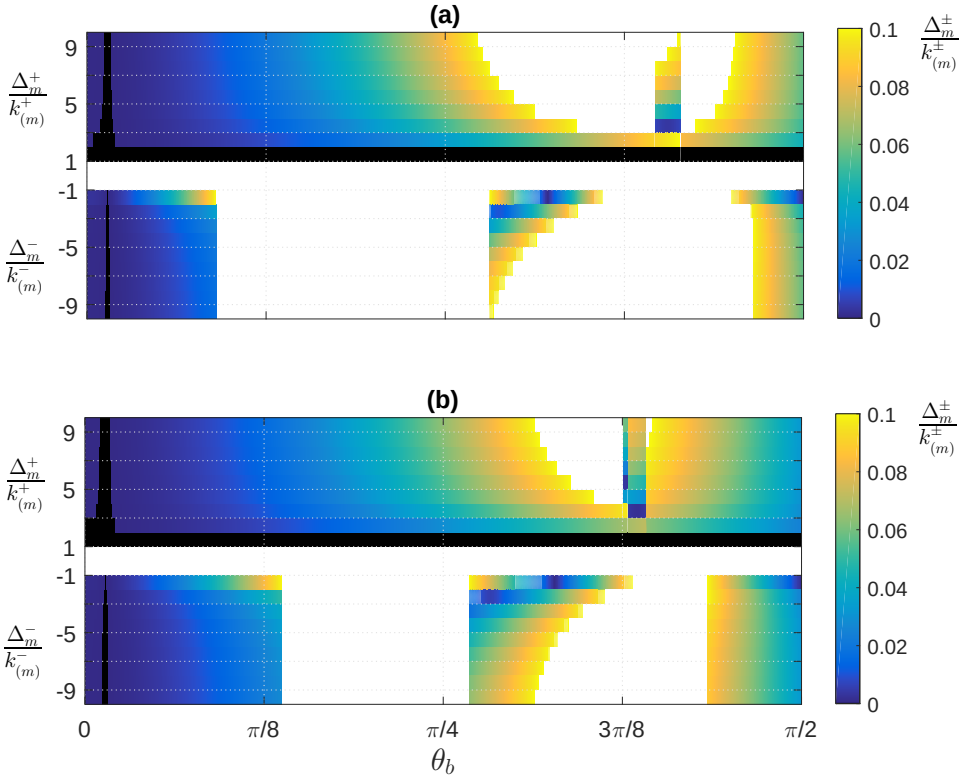

FIGURE 5. Same as figure 4, except that this time k_b is chosen such that (a) $k^+_{(1)} = k_3$ and (b) $k^+_{(1)} = k_4$.

The variations of the wave amplitudes over the corrugated patch are shown in figure 6 for small bottom angles $\theta_b = 0$ (left figures) and $\theta_b = \pi/9$ (right figures), and for wavenumbers $k^+_{(1)} = k_2$ (top figures) and $k^+_{(1)} = k_4$ (bottom figures). For the two cases of small wavenumber $k^+_{(1)} = k_2$ (i.e. figures 6a,b), the detuning for the first resonated wave A^-_1 is so large, i.e. $\Delta^-_1/k^-_{(1)} > 10\%$ (c.f. figure 4), that all A^-_m waves are neglected. The chain resonance remains nonetheless infinite for $\theta_b = 0$ (figure 6a), because all A^+_m waves are very close to resonance. As a result, the incident wave decreases monotonically over the patch. For $\theta_b = \pi/9$ (figure 6b), the picture becomes significantly different over relatively long distances (we show this case over a larger corrugated domain to see this), because the cumulative detuning grows relatively rapidly such that it exceeds 2% for $m > 8$. This increase in detuning results in high-wavenumber internal waves that are unable to capture the incident wave energy, which increases again from $x/\lambda_1 = 40$ onward. In the case where $k^+_{(1)} = k_4$ (figure 6c,d), the detuning of A^-_m waves is small, i.e. $\Delta^-_m/k^-_{(m)} < 10\%$, such that a relatively large number of reflected waves can be seen to grow from the downstream toward the upstream (solid-dotted lines). The detuning $\Delta^-_m/k^-_{(m)}$ is however non-negligible for $\theta_b = \pi/9$ (figure 6d), such that the fraction of incident wave energy going to the A^-_m waves is substantially less than in the case of $\theta_b = 0$. It is to be noted that the patch length in figures 6c,d was truncated to just half of figure 6a, because the generation of the resonated waves is much faster when the corrugations are short (see how A^+_1 increases faster in figure 6c than in figure 6a). The very high-wavenumber internal waves (typically greater than mode 10) shown in figure 6 may not be accurately captured by the theory because they do not satisfy the long

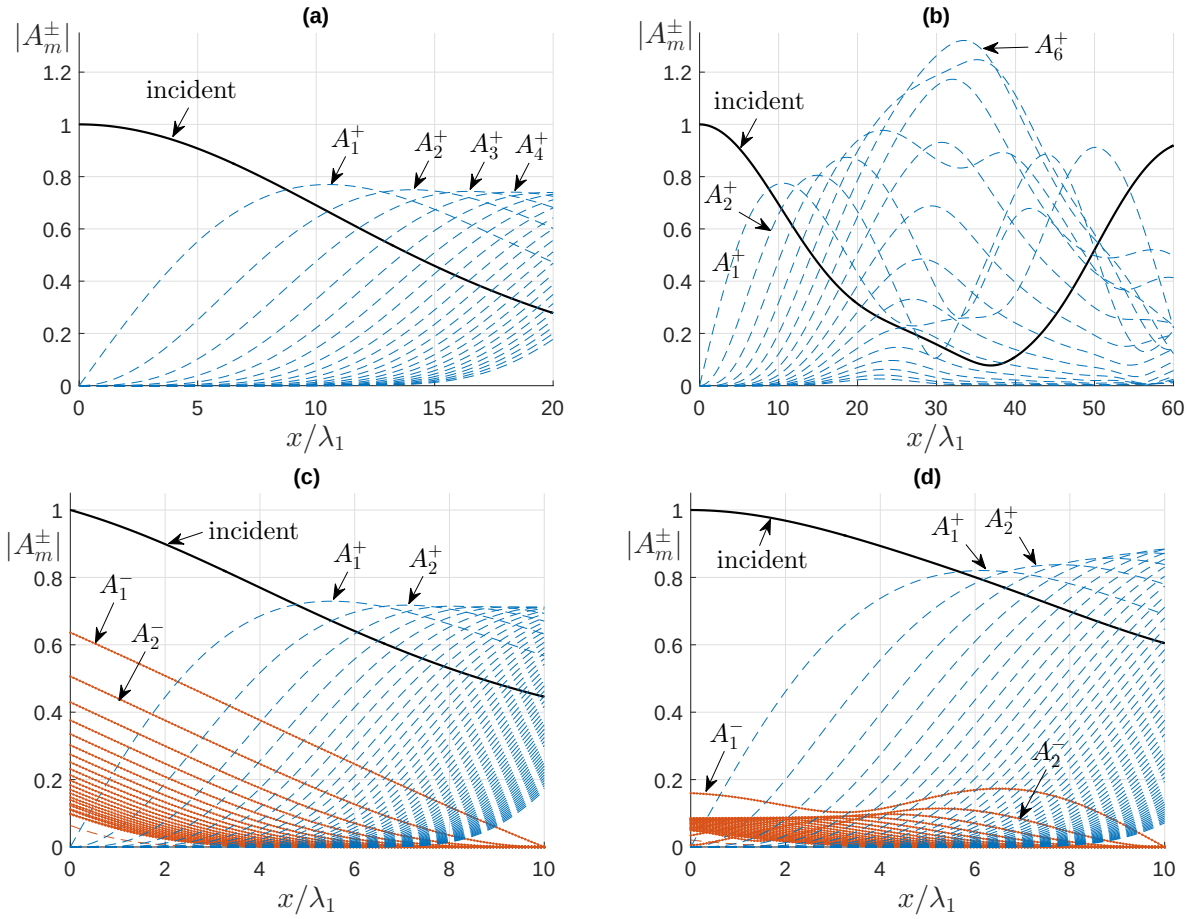

FIGURE 6. Evolution of the envelope amplitudes of the $k^+_{(m)}$ waves (dash-dash line) and $k^-_{(m)}$ waves (solid-dotted line), for corrugation angle $\theta_b = 0$ (a,c) and $\theta_b = \pi/9$ (b,d). The bottom wavenumber is selected such that $k^+_{(1)} = k_2$ for the top two figures (a,b), in which case there are no $k^-_{(m)}$ waves because the detuning $\Delta^-_1/k^-_{(1)} > 10\%$ (c.f. figure 4). For the bottom two figures (c,d), $k^+_{(1)} = k_4$, such that reflected $k^-_{(m)}$ waves with smaller detuning $\Delta^-_m/k^-_{(m)} < 10\%$ can be seen. In figures (c) and (d) we select a normalized patch length of $l/\lambda_1 = 10$, i.e. half the patch length in figure (a), because the generation of the resonated waves is much fast in figures (c) and (d). In figure (b), on the other hand, we select a longer domain, i.e. $l/\lambda_1 = 60$, to show that the wave modulation is quasi periodic. In (a) we show the first 20 waves, but convergence requires $M^+ = 50$. In (b), we show the first 15 waves and convergence is secured with $M^+ = 15$. In (c) and (d) we show the first 50 $k^+_{(m)}$ and 20 $k^-_{(m)}$ waves but we need $M^+ = 100$ and $M^- = 40$ to achieve convergence. The physical parameters are the same as those of figure 3.

vertical wavelength condition $D\gamma \ll 1$ (see §2.2 and equation (2.6)). Nonetheless, the chain resonance is still expected to occur, such that only the details of the energy exchanges should differ using a higher-order theory or direct simulation.

Another particularly interesting case occurs when the corrugation crests are perpendicular to the incident wave crests, i.e. such that $\theta_b = \pi/2$ (*iv* in figure 4). In a homogeneous fluid, such an orientation of the seabed bars with respect to the incident waves does not lead to any type of Bragg resonance interaction because the solutions (k, ω) of the dispersion relation all fall on a unique circle. In a stratified fluid, however, there are infinite wavenumber solutions of the dispersion relation such that an incident mode-one internal wave can resonate higher-mode internal waves via perpendicular bottom corrugations. We show in figure 7 the

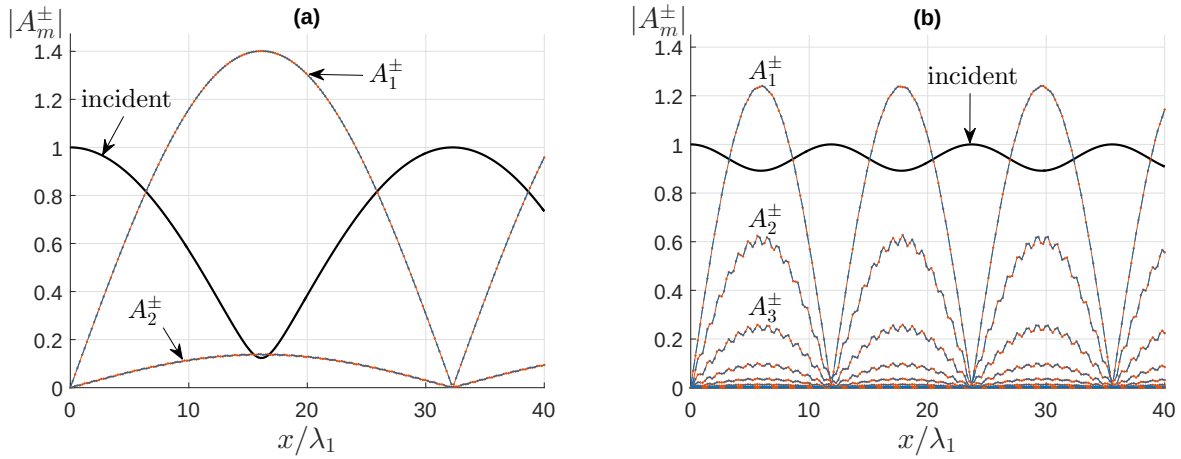

FIGURE 7. Evolution of the envelope amplitude of the $k^+_{(m)}$ waves (dash-dash line) and $k^-_{(m)}$ waves (solid-dotted line) over a patch of length $l = 40\lambda_1$. The corrugation angle is $\theta_b = \pi/2$ such that the wave amplitudes overlap, i.e. $A^+_m = A^-_m$. The bottom wavenumber is selected such that (a) $k^+_{(1)} = k_2$ and (b) $k^+_{(1)} = k_4$. In (a) we show the first two pairs of resonated waves only, because all other waves have detuning greater than 10%. In (b), we show the first 10 waves for which convergence is secured; for $m = 5$, $\Delta^{\pm}_m/k^{\pm}_{(m)} > 3\%$ such that any further ($m \geq 5$) resonated wave does not capture much energy. The physical parameters are the same as those of figure 3.

variations of the wave envelopes along the x axis when the $k^+_{(1)}$ wave is a mode-two (figure 7a) or mode-four internal wave (figure 7b). The resonance conditions for the $k^+_{(m)}$ and $k^-_{(m)}$ waves are similar in this case (i.e. the only difference is $\theta^+_m = -\theta^-_m$), such that the wave amplitudes A^+_m and A^-_m overlap. For $k^+_{(1)} = k_2$, the detuning is $\Delta^{\pm}_m/k^{\pm}_{(m)} > 10\%$ for $m > 2$, such that we consider only four $(1^+, 2^+, 1^-, 2^-)$ resonated waves in the chain resonance (see figure 7a). The exchange of energy between the incident wave and the two pairs of resonated waves is clearly oscillatory. This is because (i) all waves propagate in the $+x$ direction, and (ii) there is only a finite number of waves that are resonated. The oscillatory behavior is also obtained in figure 7b, for $k^+_{(1)} = k_4$, but this time the detuning decreases such that more waves enter the chain resonance. Interestingly, we see that the larger number of resonated waves in figure 7b leads to a smaller minimum of the incident wave amplitude. This is a direct result of the conservation of wave action (3.13), which requires the energy flux to be conserved. In figure 7b, the resonated waves carry a much smaller energy flux $\hat{x} \cdot \mathbf{F}^{\pm}_m$ in x direction (c.f. (3.15)), compared to the waves in figure 7a, because of their higher wavenumbers and larger angle with respect to the x axis. As a result, much less energy is needed from the incident wave to maintain the equilibrium between the resonated waves in figure 7b than in figure 7a.

In order to provide an independent cross-validation of the occurrence of chain resonance, we now show in figure 8 the evolution of the envelope amplitudes of the incident wave and first four resonated waves as predicted by multiple-scale theory and direct simulation. We solve the full Euler's equation under Boussinesq approximation with MITgcm (*Marshall et al.*, 1997), an open source non-hydrostatic hydrodynamic solver (finite volume) widely used for modeling waves in stratified fluids (e.g. *Engqvist and Hogg*, 2004; *Klymak et al.*, 2010; *Lim et al.*, 2010; *Churaev et al.*, 2015; *Alford*, 2015). Our main interest lies in verifying that the waves that are predicted to resonate by the theory become also resonated when using MITgcm, and that the strength of the interaction is similar for the two methods. Therefore, we solve the initial-value problem (i.e. $\partial_{\bar{x}} \equiv \partial_{\bar{y}} \equiv 0$) rather than the boundary-value problem for the ease of computation. With internal waves of different wavelengths and directions of propagation, the implementation of radiation boundary conditions or sponge layers remains challenging. An alternative based on a numerical domain large enough that reflections from boundaries do not matter could be more easily set up, but this is unfortunately not practical computationally. We consider a mode-one internal wave propagating without change of form in $+x$ direction for $t < 0$, until bottom corrugations suddenly appear at $t = 0$, subsequently scattering the incident mode-one wave energy for $t > 0$. The bottom corrugation angle is selected such that the corrugation crests

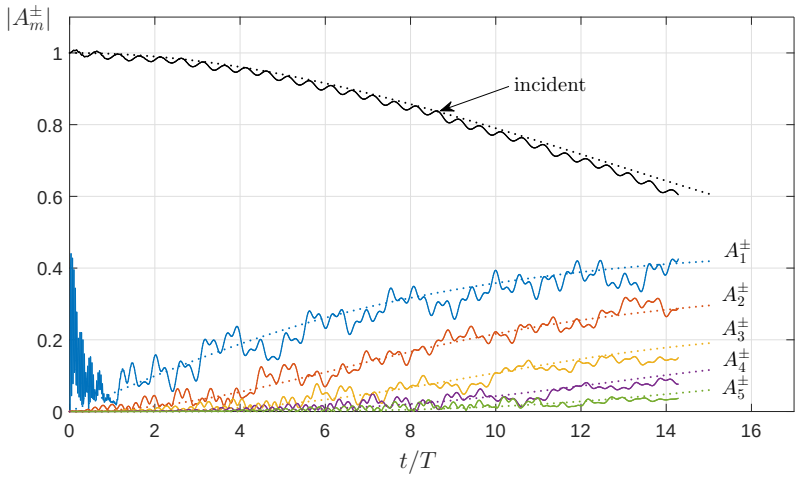

FIGURE 8. Evolution of the envelope amplitudes for the incident wave and for the first five resonated waves as predicted by multiple-scale theory (dotted lines), and by direct numerical simulation using MITgcm (solid lines). We solve the initial-value problem such that $A_0 = 1$ and $A_m^{\pm} = 0$ $(m > 0)$ at $t = 0$. The corrugation angle is $\theta_b = \pi/2$ such that $A_m^{+} = A_m^{-}$ $\forall m$, and the bottom wavenumber is chosen such that the first resonated wave is a mode-three internal wave ($k_{(1)}^{+} = k_3$). The numerical domain contains 400×400 grid points for a domain size $2\lambda_1 \times 2\lambda_1$ in x, y direction, and we use 100 layers along the fluid depth which we take equal to 100 meters. The time step is 0.1 s. The physical parameters are chosen such that $\omega/N = 0.2$, $ha = 0.05$, $d/h = 0.05$, and the Coriolis parameter is set to zero. The initial mode-one wave amplitude in MITgcm is 1 meter.

are perpendicular to the incident wave crests, i.e. $\theta_b = \pi/2$, and we pick k_b such that $k_{(1)}^{+} = k_3$. The multiple-scale solution for the initial-value problem is readily obtained from the solution method described for the boundary-value problem, provided that the diagonal elements of matrix $[E]$ are substituted with $\Omega_m^{\pm}$ (c.f. equation (3.23)). The boundary conditions are $A_0 = 1$ at $t = 0$, and $A_m^{\pm} = 0$ $(\forall m > 0)$ at $t = 0$. In the numerical setup, we use a free-surface and a free-slip bottom boundary condition, and we turn off viscosity. The envelope amplitudes are extracted from the free-surface elevation data using discrete Fourier transform in both x and y at successive time steps. Figure 8 shows that the multiple-scale predictions compare well with the converged direct simulation results for the first five resonated modes that are shown, endorsing the discussed trend of energy flowing to higher-wavenumber internal waves as time progresses. We do not, however, have a physical explanation for the rapid oscillations of the first resonated internal waves $A_1^{\pm}$ at the very beginning of the simulation. This feature is not predicted by multiple scales and therefore we speculate that it is a non-physical and transient artifact of the direct simulation scheme. This large discrepancy at $t \sim 0$ may be at the origin of the differences with the multiple-scale results observed at later times. Other effects, however, due to higher wave-bottom interactions and wave-wave nonlinearities considered in the direct simulation, may also explain the small deviations from the theory. Importantly, the good agreement between the two methods proves that the condition $D\gamma \ll 1$ on the vertical wavelength of the internal waves can be relaxed (see §2.2 and equation (2.6)), at least in this case. Indeed, here we show a good agreement up to the $k_{(5)}^{\pm}$ waves, which are mode-fifteen internal waves. These waves have small vertical wavelengths, i.e. $\gamma_{(5)}^{\pm} = \gamma_{15} \sim 15\pi/h$ such that $D\gamma \sim 2.5$. They are therefore beyond the validity range of the assumption, but nonetheless well predicted by the theory. We would like to note that discrepancies other than those due to nonlinear effects could be obtained when solving the boundary-value problem. Indeed, with oblique seabed corrugations, the water depth is discontinuous at the beginning and end of the corrugated patch, such that waves reflected by abrupt seabed steps can be obtained in the numerical experiments. However, with seabed steps less than 5% the height of the water column, such reflections should stay small, hence dominated by the leading-order phenomenon of chain resonance.

4.4. **Energy flux redistribution.** In this section, we further investigate the effect of the corrugation angle on the dynamics of chain resonance by showing the decay of the incident wave energy over the patch, and by evaluating the maximum amount of energy captured by the resonated waves for different corrugation angles.

We first show in figure 9 the variations of the normalized energy flux of the incident wave, i.e. $\mathcal{F}_0(x)/\mathcal{F}_0(x=0)$ where $\mathcal{F}_0 = \|\mathbf{F}_0\|_2$ (see equation (3.15)) over the corrugated patch, obtained for 100 different corrugation angles θ_b taken uniformly in $[0,\ \pi/2]$ (dark to bright solid lines). To highlight the importance of chain resonance, we show the *naive* results, i.e. obtained with only one resonated wave (A_1^+) considered in the chain resonance such that $M^+ = 1$, $M^- = 0$ (see equation (3.23)), for $k^+_{(1)} = k_2$ in figure 9a and for $k^+_{(1)} = k_4$ in figure 9c. The energy flux simply oscillates in these two cases with a period increasing with the corrugation angle θ_b. This is because the resonated wave A_1^+ encounters fewer corrugation crests along the length of the patch in x direction when θ_1^+ (and θ_b) is increased.

The effect of the other higher-wavenumber resonated waves on the decay of the incident energy flux can be seen in figure 9(b,d), which show the same results as in (a,c) except that this time we consider all resonated waves. The incident energy flux does not simply oscillates anymore, but shows a relatively complex behavior that is sensitive to whether the corrugations are long (figure 9b) or short (figure 9d). In figure 9b, the energy flux decreases monotonically over the patch for small corrugation angle (shown by dark lines), because the incident wave energy keeps going to higher and higher-wavenumber resonated waves (as already discussed in figure 6). As the corrugation angle increases and becomes larger than about $\pi/9$, however, the incident energy flux becomes oscillatory again due to the fact that the chain resonance only includes a finite number of near-resonance waves (which corresponds to the situation shown in figure 6b). The variations of the incident energy flux are thus relatively similar for large angle θ_b in both figures 9a,b (shown by bright-colored lines). In figure 9d, similar features can be observed as for figure 9b, although the differences with the *naive* results (shown in figure 9c) are even more emphasized. For large corrugation angle $\theta_b \sim \pi/2$ (bright-colored lines), for instance, the incident energy flux oscillates but in the case of figure 9d the minimum reached remains large, i.e. close to 1 (contrary to figure 9b in which the minimum is close to 0). This is due to the fact that the resonated waves included in the chain resonance propagate at a large angle with respect to the x axis when the corrugations are relatively shorter, as discussed in figure 7b, thus carrying less energy in x direction.

In order to estimate how the incident wave energy is redistributed across the internal wave spectrum for the different corrugation parameters used in figure 9, we now show in figure 10 the maximum normalized energy flux $\mathcal{F}^{\pm}_m(x)/\mathcal{F}_0(x=0)$ reached over the patch by the resonated waves. For each corrugation angle, a unique chain resonance is obtained that is represented as a trajectory in wavenumber space $(k_x h, k_y h)$ starting from the incident wavenumber $\mathbf{k}_{(0)}h = (k_1 h, 0)$; each trajectory is color coded by the intensity of the energy flux of the resonated waves $\mathbf{k}^{\pm}_{(m)}h$ in the chain resonance. In figure 10a,c we consider only one resonated wave (A_1^+) in the chain resonance, such that each trajectory consists of one segment connecting the incident wavenumber $\mathbf{k}_{(0)}h$ to the resonated wavenumber $\mathbf{k}^+_{(1)}h$. The intensity of the energy flux $\max_x \mathcal{F}_1^+(x)/\mathcal{F}_0(x=0)$ is clearly seen to smoothly increase as θ_b increases in this case (as the trajectory goes from being parallel to the x axis to being perpendicular), which is due to the fact that the total energy flux needs to be conserved in x direction and that the incident energy flux becomes 0 somewhere along the patch (see figure 9a,c), i.e. such that $\max_x \mathcal{F}_1^+(x)\cos\theta_1^+ = 1$ where θ_1^+ increases with θ_b. Figure 10a and 10c differ only in that the corrugation wavenumber is larger in the later figure, such that the resonated wave has a higher wavenumber $k^+_{(1)} = k_4$ for the case of figure 10c compared to $k^+_{(1)} = k_2$ for the case of figure 10a.

When all resonated waves are considered (figure 10b,d), the trajectories consist of many segments connecting each successively resonated waves. The trajectories can include *positively* generated waves $k^+_{(m)}$ (shown by branches in the upper right quadrant), but also *negatively* generated waves $k^-_{(m)}$ (shown by branches in the lower left quadrant). In figure 10b, the *positive* branches of the trajectories are very long (i.e. including more than 10 resonated waves) for a wide range of corrugation angle ($\theta_b \lesssim 3\pi/8$) because the detuning $\Delta^+_m/k^+_{(m)}$ is small in this case (see figure 4). As the corrugation angle is increased ($\theta_b \gtrsim 3\pi/8$), however, the detuning also increases such that some of the higher-wavenumber generated waves become neglected, resulting in truncated *positive* branches (as seen by the stair-case shape in the upper right quadrant of figure 10b). For a narrow range of corrugation angles near $\theta_b \sim 0$, the trajectories also have a *negative* branch (shown as *ii* in figure 10b), with a fraction of the incident wave energy transferred toward reflected internal waves via the surface wave mode k_0. The maximum energy flux of the surface wave is substantial (about 0.3)

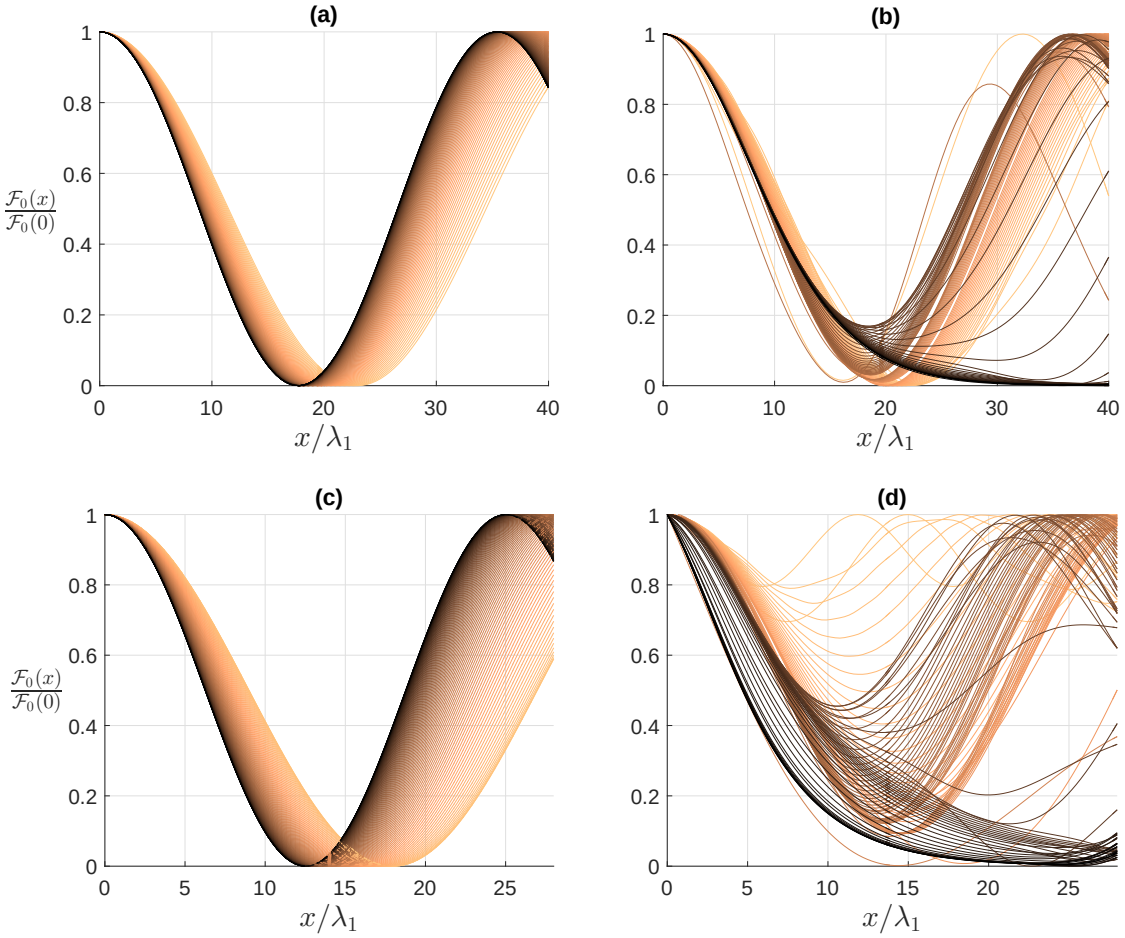

FIGURE 9. Variations of the normalized incident wave energy flux $\mathcal{F}_0(x)/\mathcal{F}_0(x=0)$ over the patch for 100 different corrugation angles $\theta_b \in [0,\ \pi/2]$ (shown by solid lines from dark to bright). The corrugation wavenumber k_b is chosen such that (a,b) $k^+_{(1)} = k_2$, and (c,d) $k^+_{(1)} = k_4$. The plots on the left show the *naive* results obtained with only one resonated wave (A^+_1) included in the chain resonance ($M^+ = 1,\ M^- = 0$), whereas the plots on the right are obtained with all resonated waves considered [$M^+ = M^- = 40$ for (b), $M^+ = M^- = 80$ for (d)]. The physical parameters are the same as those of figure 3.

in this case, despite the fact that the surface-wave amplitude grows only by about $1/100^{th}$ of the incident wave amplitude; this is a result of the much higher group velocity of the surface mode (see related discussion in §4.2). A *negative* branch of the trajectories is also obtained when $\theta_b \sim \pi/2$ (*iv* in figure 10b; see also discussion of figure 7), and when θ_b is given by equation (4.1) (*iii* in figure 10b), which is the somewhat special case that includes three perfect resonant waves discussed in §4.1. For $\theta_b = \theta_b^*$ (c.f. equation (4.1)), the two perfectly resonant waves $k^-_{(1)}, k^-_{(2)}$ reach a small maximum normalized energy flux (about 0.07), which can readily be inferred from the plot of the wave amplitudes in figure 3b. For θ_b slightly less than θ_b^* (i.e. decreased by about 1%), the same two waves are slightly detuned, but remarkably reach a very large maximum energy flux of $\max_x \mathcal{F}^-_m(x)/\mathcal{F}_0(x=0) \sim 3.1, 2.6$ for $m = 1, 2$ (shown by the bright *negative* branch near *iii* in figure 10b), i.e. amplified by about two orders of magnitude. The resonance dynamics is thus significantly enhanced with small detuning, which is a behavior that can be also obtained in nonlinear wave-wave systems (see e.g. *Dutykh and Tobisch*, 2014). In order to further characterize the effect of a small change of the corrugation angle on the dynamics of the cluster resonance, we show the evolution of the wave amplitudes for the case shown in figure 3b (i.e. $\theta_b = \theta_b^* = 0.9125$, c.f. (4.1)) and for $\theta_b = 0.9055$ in figure 11. The order of magnitude increase of the two resonated waves (A^-_1 and A^-_2) between the two cases,

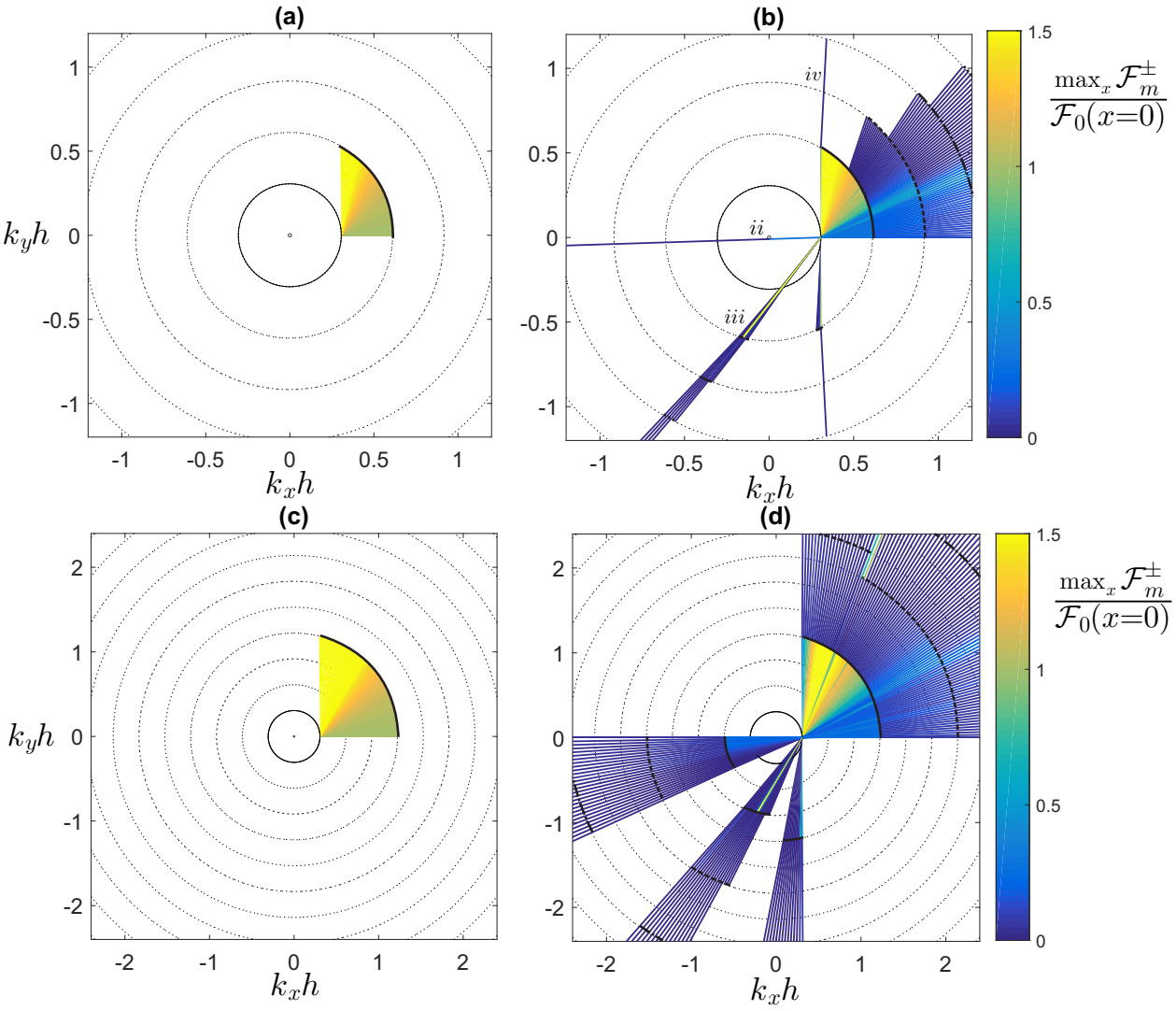

FIGURE 10. Normalized maximum wave energy flux $\mathcal{F}_m^{\pm}/\mathcal{F}_0(x=0)$ of the resonated waves in chain resonance with (a,b) $k_{(1)}^{+} = k_2$, and (c,d) $k_{(1)}^{+} = k_4$, for 100 different corrugation angles $\theta_b \in [0,\ \pi/2]$ (i.e. same as in figure 10). The chain resonance trajectories are plotted in $(k_x h, k_y h)$ space and colorcoded with the intensity of the maximum normalized energy flux. In (a,c), where only one resonated wave (A_1^{+}) is considered in the chain resonance, the trajectory emanates from the incident wavenumber $\mathbf{k}_{(0)}h = (k_1 h, 0)$ and reaches out to $\mathbf{k}_{(1)}^{+}h$ with the colorcode given by $\max_x \mathcal{F}_1^{+}/\mathcal{F}_0(x=0)$. In (b,d), the trajectories include all successively generated waves at and near resonance. The maximum normalized energy flux does not increase monotonically with the corrugation angle θ_b in this case, and can be relatively large even for some of the higher-wavenumber waves (i.e. $k_{(m)}^{\pm}$, $m > 1$). The roman numerals in (b) refer to the same features shown in figure 5 that are further discussed in the text. The dotted circles represent the internal wavenumber $k_j h$ solutions of the dispersion relation (2.9). The patch length and the physical parameters are the same as in figure 9.

which differ by less than 1% relative change in θ_b, can be clearly seen (c.f. figure 11a and b). We would like to remark that the conservation of energy flux in x direction is not violated in the case of enhanced detuned resonance even though the energy flux of the two amplified waves exceeds the incident energy flux

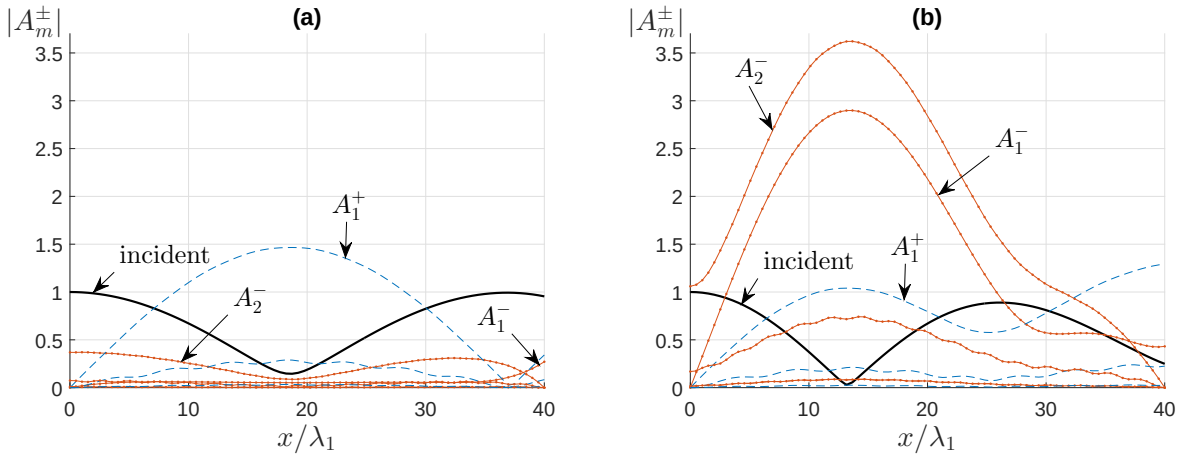

FIGURE 11. Evolution of the envelope amplitudes of the $k^+_{(m)}$ waves (dash-dash line) and $k^-_{(m)}$ waves (solid-dotted line), for corrugation angle (a) $\theta_b = \theta_b^*$ (c.f. (4.1)), and (b) $\theta_b = 0.9928\theta_b^*$. The small decrease ($< 1\%$) of the corrugation angle from figure (a) to figure (b) results in detuned $k^-_{(1)}$ and $k^-_{(2)}$ waves (they are perfectly tuned for $\theta_b = \theta_b^*$ in (a)), which yet grow by one order of magnitude larger than in figure (a). The patch length is $l = 40\lambda_1$ and all other parameters are the same as in figure 3.

($\max_x \mathcal{F}_m^-(x)/\mathcal{F}_0(x=0) \sim 8.4, 6.6$ for $m = 1, 2$ in figure 11b); the two waves A_1^- and A_2^- propagate in opposite x direction such that they cancel each other.

Figure 10c,d show results similar to figure 10a,b for shorter corrugations, i.e. such that $k^+_{(1)} = k_4$. As already discussed in figure 5b, the detuning is smaller in this case such that many more resonated waves are included in the chain resonance. Figure 10d thus shows longer trajectories than in figure 10b, in particular for the *negative* branches in the lower left quadrant, which consists mostly of reflected internal waves. An enhanced detuned resonance can also be observed, as shown by the bright-colored trajectory in the lower left quadrant of figure 10d.

4.5. **Generalization of the results to arbitrary physical parameters.** As mentioned at the beginning of §4, the results presented in this paper were obtained for fixed physical parameters while varying the angle and wavelength of the bottom corrugations. The effect of the corrugation amplitude d/h is well known in the weak-topography limit, i.e. the energy transfer rate scales linearly with d/h, and therefore we could fix d/h without loss of generality. How the results might change with the internal wave frequency, buoyancy frequency, or water depth is however of significant interest since the oceans experience very different physical conditions.

The effect of varying physical parameters can be understood by looking at the interaction coefficients between the incident and resonated waves, which are given by the diagonal elements of matrix $[E]$ (c.f. (3.22)):

$$r_m^{\pm} = \lambda_1 \Omega_m^{\pm}/C_{gmx}^{\pm} = \frac{d}{2h}\frac{2\pi}{\cos\theta_m^{\pm}}\frac{\gamma^{\pm}_{(m)}h}{\gamma_1 h}\frac{1}{1+\frac{\sin 2\gamma^{\pm}_{(m)}h}{2\gamma^{\pm}_{(m)}h}}. \tag{4.4}$$

The coefficient $r_m^{\pm}$ in (4.4) is non-dimensionalized by λ_1, and represents the growth (or decay) rate of wave $A_m^{\pm}$ per unit incident wavelength. As can be seen in figure 12 where we plot $r_m^{\pm}$ as a function of $\gamma^{\pm}_{(m)}h$ ($\theta_m^{\pm} = 0$), $r_m^{\pm}$ is asymptotically proportional to $\gamma^{\pm}_{(m)}h$, with small oscillations apparent due to the consideration of a free-surface. The interaction coefficient $r_m^{\pm}$ indeed reduces to

$$r_m^{\pm} = 2\pi\frac{d}{2h}\frac{\gamma^{\pm}_{(m)}h}{\gamma_1 h}, \tag{4.5}$$

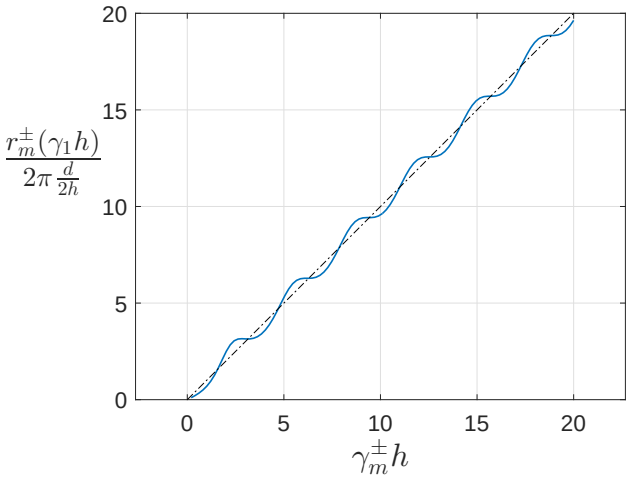

FIGURE 12. Rate of change of the interaction coefficient $r_m^{\pm}$ (c.f. equation (4.4)) with the normalized vertical wavenumber $\gamma_m^{\pm} h$ for $\theta_m^{\pm} = 0$. As shown by the dash-dotted line (which represents $r_m^{\pm}$ obtained under rigid-lid assumption, c.f. (4.5)), $r_m^{\pm}$ is asymptotically proportional to $\gamma_m^{\pm} h$, which implies that the free-surface results are similar to the rigid-lid results, and that the energy exchanges are faster for higher-wavenumber internal waves.

under rigid-lid assumption (as shown by the dash-dotted line in figure 12), which, given that $\gamma_{(m)}^{\pm}/\gamma_1$ is an integer number (with rigid-lid), is independent of the physical parameters (*Bühler and Holmes-Cerfon*, 2011). Here, the variations of $r_m^{\pm}$ with the physical parameters are due to the effect of the free-surface and are strongest for the first few interactions. However, for practical physical conditions, i.e. $\omega/N \in [f/N,\ 1]$ and $ha \in [0,\ 0.05]$, we find that the relative variations of $r_m^{\pm}$ are on the order of only 1%, hence negligible. It is to be noted that the quasi-linear increase of $r_m^{\pm}$ with the normalized vertical wavenumber $\gamma_{(m)}^{\pm}/\gamma_1$ is consistent with the rapid generation of high-wavenumber internal waves over the corrugations, as was clearly seen for small θ_b in figure 6a,c.

The above analysis demonstrates that the rapidity of the energy exchanges are basically proportional to $(1/\lambda_1) \propto \mu/h$, hence increases with decreasing water depth and increasing wave frequency. The results presented in §4.1-§4.4 holds for a broad range of physical parameters, and therefore could be in theory applicable for internal waves on the continental shelf or in the abyss. It is to be noted that the main variations of the energy transfer rates are affected by the complex effect of detuning, oblique interactions and the Coriolis force, which are represented by matrix $[D]$, $[S]$, and $[F]$ in equation (3.22). In brief, the effect of detuning results in faster but weaker modulations of the energy transfers, whereas the effect of the Coriolis force and oblique interactions, which similarly result in modified modulation patterns, are only important for relatively large angles between the incident wave and bottom corrugations.

We would like to finally point out that the the spatial dynamics of chain resonance is dependent on the length of the corrugated patch when some of the resonated waves are reflected. The effect of a varying patch length can change the modulation of the wave amplitudes, especially when the parameters are chosen close to a case of enhanced detuned resonance. For physical parameters as in figure 11b, but for a patch half as long, for instance, i.e. ending at $x/\lambda_1 = 20$, A_1^- and A_2^- reach a maximum of 2.1 and 1.6 respectively, both approximately 40% smaller than what is obtained in figure 11b, such that the dynamics is significantly sensitive to the length of the patch. This is however not the general case since the reflected waves do not play a major role for most of the corrugation angles θ_b, in particular when the corrugations are long, i.e. such that $k_{(1)}^{+} = k_2$ (see figure 10b). Effects due to the patch length as well as due to other types of reflective boundaries may yet display new interference patterns which could be interesting (see e.g. *Karimpour et al.*, 2016).

5. Concluding remarks

In this work, we showed that an incident internal wave propagating over oblique bottom corrugations can resonate a large number of other freely propagating waves for a wide range of physical conditions. We explained that this behavior results from the occurrence of chain resonance, whereby a single seabed harmonic can resonate many different interconnected wave triads. The concept of chain resonance has its roots in the broader context of nonlinear wave science and resonance cluster (*Tobisch*, 2016), to which it is a special case as one wave in each triad is a frozen (medium) wave whose amplitude is fixed. We demonstrated that the chain resonance occurs for incident internal wave and corrugation crests that are either aligned or perpendicular, as well as for all other angles of the bottom corrugations. The chain resonance mechanism can efficiently redistribute the internal wave energy in the two-dimensional horizontal wavenumber spectrum, thus potentially contributing to enhanced mixing and energy dissipation. We showed that near-resonance waves cannot be neglected, and that the solutions to the boundary-value problem can be significantly sensitive to the corrugation angle. With changes of the corrugation angle as small as $0.01°$, we found that the system can experience an enhanced detuned resonance, i.e. such that waves that become slightly detuned experience order of magnitude amplification and dominate the internal wave field. Waves with relatively large detuning, but that can still be predicted by the multiple-scale method, on the other hand, are not predicted to play a major role in the internal wave dynamics. This suggests that the multiple-scale model captures the most important features of the chain resonance.

The shortcoming of uniform density stratification that was assumed in this paper has been addressed in a number of earlier studies on internal wave scattering by bottom corrugations (*Bühler and Holmes-Cerfon*, 2011), which, based on the results of *Grimshaw et al.* (2010), argued that the fundamental ways in which the interactions occur do not change for depth-dependent stratification. Although realistic density profiles deserve attention, here we believe that the chain resonance is also relevant to other density profiles, in particular because the successively forced waves are never perfectly resonant. In fact it is not unreasonable to speculate that an ocean with a variable stratification, and therefore non-uniformly spaced wavenumbers, could have stronger energy transfers toward high-wavenumber waves for oblique incidence than in the constant stratification case due to better tuned resonance.

Even though our results were presented for a single seabed harmonic, the theory can be easily extended to multiple corrugation wavenumbers, in which case one can expect a ramification of the chain resonance across the two-dimensional wavenumber space. The number of resonant branches may in fact become infinite with just two seabed harmonics and may exhibit interesting different wave dynamics. To extend the range of applicability of the theory to more general cases, finite-amplitude bottom corrugations should be considered and are worth independent investigation. However, large seabed variations require higher-order or exact linear wave theories, such as Green functions approach or Floquet theory, making the problem much less tractable analytically (see e.g. in homogeneous water *Yu and Howard*, 2012). Numerical simulations could obviously be used but we shall recall that the problem investigated here is three-dimensional and therefore computationally intensive.

The redistribution of energy across the internal wave spectrum is of significant importance in order to predict enhanced mixing efficiency and wave breaking near topography. Therefore, it will be essential to include the effect of finite-amplitude internal waves in future studies. Nonlinear wave-wave effects will be most likely increased by and coupled to the internal wave dynamics of chain resonance over seabed corrugations.

Appendix A. Derivation of the linear internal wave equation

Here we derive the linear wave equation (2.2) for the vertical velocity starting from the Boussinesq equation (2.1). Similar to the density perturbation ρ', we define a pressure perturbation p' via $p = \bar{p}(z) + p'(x, y, z, t)$ such that $d\bar{p}(z)/dz = -\bar{\rho}(z)g$. The calculation $\partial_z\partial_x[(\partial_t + f)(2.1\mathrm{a})_1] + \partial_z\partial_y[(\partial_t + f)(2.1\mathrm{a})_2] - \partial_t\nabla_H^2(2.1\mathrm{a})_3$, where $(2.1\mathrm{a})_{1,2,3}$ denote the x, y, z components of (2.1a) and where $\nabla_H^2 = \partial_x^2 + \partial_y^2$ is the horizontal Laplacian, yields

$$\partial_t\nabla^2 w + f^2\partial_{zz}w + \frac{g}{\rho_0}\partial_t\nabla_H^2\rho' = 0. \tag{A.1}$$

The density term ρ' can be readily substituted from the linear form of (2.1b), i.e.,

$$\partial_t \rho' + w \frac{d\bar{\rho}(z)}{dz} = 0, \tag{A.2}$$

such that, denoting by $N^2 = -g/\rho_0 \mathrm{d}\bar{\rho}(z)/\mathrm{d}z$ the Brunt-Väisälä frequency, (A.1) becomes

$$\partial_t \nabla^2 w + f^2 \partial_{zz} w + N^2 \nabla_H^2 w = 0, \tag{A.3}$$

which is the linearized field equation (2.2a). To obtain the free-surface boundary condition for w, i.e. (2.2b), we consider the linear form of (2.1e), i.e.

$$\partial_t p' - w\rho_0 g + \eta \partial_{tz} p' - \rho_0 g \eta \partial_z w + \eta w \rho_0 N^2 = 0, \text{ at z} = 0. \tag{A.4}$$

A second expression including p' can be derived by taking the x derivative of $\partial_t(2.1\mathrm{a})_1 + f(2.1\mathrm{a})_2$ added to the y derivative of $\partial_t(2.1\mathrm{a})_2 - f(2.1\mathrm{a})_1$, such that

$$-\partial_t^2 \partial_z w - f^2 \partial_z w + \nabla_H^2 \partial_t p'/\rho_0 = 0. \tag{A.5}$$

Substituting $\partial_t p'$ in (A.5) evaluated at $z = 0$ with its expression in (A.4) then yields

$$\partial_t^2 \partial_z w - g \nabla_H^2 w + f^2 \partial_z w = 0, \text{ at z} = 0, \tag{A.6}$$

which is the same as equation (2.2b). Finally, equation (2.2c) is the same as equation (2.1f).

References

Alam, M.-R. (2012), A new triad resonance between co-propagating surface and interfacial waves, *J. Fluid Mech.*, *691*, 267–278, doi:10.1017/jfm.2011.473.

Alam, M.-R., and C. C. Mei (2007), Attenuation of long interfacial waves over a randomly rough seabed, *Journal of Fluid Mechanics*, *587*, 73–96, doi:10.1017/S0022112007007112.

Alam, M.-R., Y. Liu, and D. K. P. Yue (2009a), Bragg resonance of waves in a two-layer fluid propagating over bottom ripples. Part II. Numerical simulation, *J. Fluid Mech.*, *624*, 225–253, doi:10.1017/S002211200800548X.

Alam, M.-R., Y. Liu, and D. K. P. Yue (2009b), Bragg resonance of waves in a two-layer fluid propagating over bottom ripples. Part I. Perturbation analysis, *J. Fluid Mech.*, *624*, 191–224, doi:10.1017/S0022112008005478.

Alford, M. H. (2003), Redistribution of energy available for ocean mixing by long-range propagation of internal waves, *Nature*, *21*(March), 159–163, doi:10.1038/nature01591.1.

Alford, M. H., J. A. MacKinnon, H. L. Simmons, and J. D. Nash (2016), Near-Inertial Internal Gravity Waves in the Ocean, *Annual Review of Marine Science*, *8*(1), 150902153948,007, doi:10.1146/annurev-marine-010814-015746.

Alford, M. H. e. a. (2015), The formation and fate of internal waves in the South China Sea, *Nature*, *521*(7550), 65–69, doi:10.1038/nature14399.

Baines, P. G. (1997), *Topographic effects in stratified flows*, Cambridge University Press.

Balmforth, N. J., G. R. Ierley, and W. R. Young (2002), Tidal Conversion by Subcritical Topography, *Journal of Physical Oceanography*, *32*(10), 2900–2914, doi:10.1175/1520-0485(2002)032¡2900:TCBST¿2.0.CO;2.

Bell, T. H. (1975), Topographically generated internal waves in the open ocean, *Journal of Geophysical Research*, *80*(3), 320–327, doi:10.1029/JC080i003p00320.

Bühler, O., and M. Holmes-Cerfon (2011), Decay of an internal tide due to random topography in the ocean, *Journal of Fluid Mechanics*, *678*, 271–293.

Bühler, O., and C. J. Muller (2007), Instability and focusing of internal tides in the deep ocean, *Journal of Fluid Mechanics*, *588*, 1–28, doi:10.1017/S0022112007007410.

Buijsman, M. C., J. M. Klymak, S. Legg, M. H. Alford, D. Farmer, J. A. MacKinnon, J. D. Nash, J.-H. Park, A. Pickering, and H. Simmons (2014), Three-Dimensional Double-Ridge Internal Tide Resonance in Luzon Strait, *Journal of Physical Oceanography*, *44*(3), 850–869, doi:10.1175/JPO-D-13-024.1.

Bustamante, M. D., B. Quinn, and D. Lucas (2014), Robust energy transfer mechanism via precession resonance in nonlinear turbulent wave systems, *Phys. Rev. Lett.*, *113*, 084,502, doi:10.1103/PhysRevLett.113.084502.

Churaev, E. N., S. V. Semin, and Y. A. Stepanyants (2015), Transformation of internal waves passing over a bottom step, *Journal of Fluid Mechanics*, *768*, 1–11, doi:10.1017/jfm.2015.92.

Couston, L.-A., M.-A. Jalali, and M.-R. Alam (2016), Shore protection by oblique seabed bars (submitted), *Journal of Fluid Mechanics*.

Davies, A. G. (1982), The reflection of wave energy by undulations on the seabed, *Dynam. Atmos. Ocean*, *6*, 207–232.

DeCarlo, T. M., K. B. Karnauskas, K. A. Davis, and G. T. F. Wong (2015), Climate modulates internal wave activity in the northern south china sea, *Geophysical Research Letters*, *42*(3), 831–838, doi:10.1002/2014GL062522.

Dutykh, D., and E. Tobisch (2014), Resonance enhancement by suitably chosen frequency detuning, *arXiv preprint*, *118*, 1–13, doi:10.1061/(ASCE)0733-950X(1992)118:1(62).

Elandt, R. B., M. Shakeri, and M.-R. Alam (2014), Surface gravity-wave lensing, *Phys. Rev. E Stat. Nonlin. Soft Matter Phys.*, *89*, 1–6, doi:10.1103/PhysRevE.89.023012.

Engqvist, A., and A. M. Hogg (2004), Unidirectional stratified flow through a non-rectangular channel, *J. Fluid Mech.*, *509*, 83–92, doi:10.1017/S0022112004009085.

Fredholm, I. (1903), Sur une classe d'équations fonctionnelles, *Acta Mathematica*, *27*(1), 365–390.

Garabato, A. C. N., K. L. Polzin, B. A. King, K. J. Heywood, and M. Visbeck (2004), Widespread intense turbulent mixing in the southern ocean, *Science*, *303*, 210–213, doi:10.1126/science.1090929.

Garrett, C., and E. Kunze (2007), Internal Tide Generation in the Deep Ocean, *Annual Review of Fluid Mechanics*, *39*(1), 57–87, doi:10.1146/annurev.fluid.39.050905.110227.

Garrett, C., and W. Munk (1979), Internal waves in the ocean, *Annu. Rev. Fluid Mech.*, *11*, 339–69.

Garrett, C., and L. St Laurent (2002), Aspects of Deep Ocean Mixing, *Journal of Oceanography*, *58*, 11–24.

Gill, A. E. (1982), *Atmosphere-ocean dynamics*, vol. 30, Academic press.

Goff, J. A., and T. H. Jordan (1988), Stochastic Modeling of Seafloor Morphology: Inversion of Sea Beam Data for Second-Order Statistics, *Journal of Geophysical Research*, *93*(B11), 13,589, doi:10.1029/JB093iB11p13589.

Grimshaw, R., E. Pelinovsky, and T. Talipova (2010), Nonreflecting Internal Wave Beam Propagation in the Deep Ocean, *Journal of Physical Oceanography*, *40*(4), 802–813, doi:10.1175/2009JPO4180.1.

Grisouard, N., and O. Bühler (2012), Forcing of oceanic mean flows by dissipating internal tides, *Journal of Fluid Mechanics*, *708*(August), 250–278, doi:10.1017/jfm.2012.303.

Guo, Y., and M. Holmes-Cerfon (2016), Internal wave attractors over random, small-amplitude topography, *Journal of Fluid Mechanics*, *787*, 148–174, doi:10.1017/jfm.2015.648.

Karimpour, F., A. Zareei, and M.-R. Alam (2016), Sensitivity of Internal Wave Energy Distribution over Seabed Corrugations to Adjacent Seabed Features, *arXiv preprint*, pp. 1–10.

Klymak, J. M., S. M. Legg, and R. Pinkel (2010), High-mode stationary waves in stratified flow over large obstacles, *J. Fluid Mech.*, *644*, 321–336, doi:10.1017/S0022112009992503.

Kranenburg, C., J. D. Pietrzak, and G. Abraham (1991), Trapped internal waves over undular topography, *J. Fluid Mech.*, *226*, 205–217, doi:10.1017/S0022112091002355.

Labeur, R. J., and J. D. Pietrzak (2004), Computation of non-hydrostatic internal waves over undular topography, *Shallow Flows*, *7*, 187–194.

Lamb, K. G. (2014), Internal Wave Breaking and Dissipation Mechanisms on the Continental Slope/Shelf, *Annual Review of Fluid Mechanics*, *46*, 231–256, doi:10.1146/annurev-fluid-011212-140701.

Ledwell, J. R., E. T. Montgomery, K. L. Polzin, L. C. St. Laurent, R. W. Schmitt, and J. M. Toole (2000), Evidence for enhanced mixing over rough topography in the abyssal ocean, *Nature*, *403*, 179–182, doi:10.1038/35003164.

Lefauve, A., C. Muller, and A. Melet (2015), A three-dimensional map of tidal dissipation over abyssal hills, *Journal of Geophysical Research: Oceans*, *120*(7), 4760–4777, doi:10.1002/2014JC010598.

Legg, S. (2014), Scattering of Low-Mode Internal Waves at Finite Isolated Topography, *Journal of Physical Oceanography*, *44*, 359–383, doi:10.1175/JPO-D-12-0241.1.

Li, Y., and C. C. Mei (2014), Scattering of internal tides by irregular bathymetry of large extent, *Journal of Fluid Mechanics*, *747*, 481–505, doi:10.1017/jfm.2014.159.

Lim, K., G. N. Ivey, and N. L. Jones (2010), Experiments on the generation of internal waves over continental shelf topography, *J. Fluid Mech.*, *663*, 385–400, doi:10.1017/S002211201000354X.

Liu, Y., and D. K. P. Yue (1998), On generalized Bragg scattering of surface waves by bottom ripples, *J. Fluid Mech.*, *356*, 297–326.

L'vov, V. S., A. Pomyalov, I. Procaccia, and O. Rudenko (2009), Finite-dimensional turbulence of planetary waves, *Phys. Rev. E*, *80*, 066,319, doi:10.1103/PhysRevE.80.066319.

Mackinnon, J. (2013), Mountain waves in the deep ocean, *Nature Oceanography*, *501*, 5–6.

Marshall, J., A. Adcroft, C. Hill, L. Perelman, and C. Heisey (1997), A finite-volume, incompressible Navier Stokes model for studies of the ocean on parallel computers, *J. Geophys. Res.*, *102*, 5753–5766, doi: 10.1029/96JC02775.

Martin, S., W. Simmons, and C. Wunsch (1972), The excitation of resonant triads by single internal waves, *J. Fluid Mech.*, *53*, 17–44, doi:10.1017/S0022112072000023.

Mathur, M., G. S. Carter, and T. Peacock (2014), Topographic scattering of the low-mode internal tide in the deep ocean, *Journal of Geophysical Research: Oceans*, *119*(4), 2165–2182, doi:10.1002/2013JC009152.

Mei, C. C. (1985), Resonant reflection of surface water waves by periodic sandbars, *J. Fluid Mech.*, *152*, 315–335, doi:10.1017/S0022112085000714.

Melet, A., M. Nikurashin, C. Muller, S. Falahat, J. Nycander, P. G. Timko, B. K. Arbic, and J. A. Goff (2013), Internal tide generation by abyssal hills using analytical theory, *Journal of Geophysical Research: Oceans*, *118*(11), 6303–6318, doi:10.1002/2013JC009212.

Muller, C. J., and O. Bühler (2009), Saturation of the Internal Tides and Induced Mixing in the Abyssal Ocean, *Journal of Physical Oceanography*, *39*(9), 2077–2096, doi:10.1175/2009JPO4141.1.

Müller, P., and N. Xu (1992), Scattering of Oceanic Internal Gravity Waves off Random Bottom Topography, *Journal of Physical Oceanography*, *22*(5), 474–488, doi:10.1175/1520-0485(1992)022¡0474:SOOIGW¿2.0.CO;2.

Munk, W., and C. Wunsch (1998), Abyssal recipes II: energetics of tidal and wind mixing, *Deep-Sea Research: Part I*, *I*(45), 1977–2010.

Nayfeh, A. H., and O. A. Kandil (1978), Propagation of waves in cylindrical hard-walled ducts with generally weak undulations, *AIAA Journal*, *16*(10), 1041–1045.

Nikurashin, M., and R. Ferrari (2010), Radiation and Dissipation of Internal Waves Generated by Geostrophic Motions Impinging on Small-Scale Topography: Application to the Southern Ocean, *Journal of Physical Oceanography*, *40*(9), 2025–2042, doi:10.1175/2010JPO4315.1.

Nikurashin, M., and R. Ferrari (2013), Overturning circulation driven by breaking internal waves in the deep ocean, *Geophysical Research Letters*, *40*(May), 3133–3137, doi:10.1002/grl.50542.

Pietrzak, J., and R. J. Labeur (2004), Trapped internal waves over undular topography in a partially mixed estuary, *Ocean Dynamics*, *54*(3-4), 315–323, doi:10.1007/s10236-003-0081-4.

Pietrzak, J. D., C. Kranenburg, G. Abraham, B. Kranenborg, and A. V. D. Wekken (1991), Internal Wave Activity in Rotterdam Waterway, *Journal of Hydraulic Engineering*, *117*(6), 738–757.

Polzin, K. (2004), Idealized solutions for the energy balance of the finescale internal wave field, *Journal of Physical Oceanography*, *34*(1), 231–246, doi:10.1175/1520-0485(2004)034¡0231:ISFTEB¿2.0.CO;2.

Polzin, K. L., J. M. Toole, J. R. Ledwell, and R. W. Schmitt (1997), Spatial variability of turbulent mixing in the abyssal ocean, *Science*, *276*(5309), 93–96, doi:10.1126/science.276.5309.93.

Schiermeier, Q. (2007), Oceanography: Churn, churn, churn, *Nature*, *447*(7144), 522–524.

St Laurent, L., and C. Garrett (2002), The Role of Internal Tides in Mixing the Deep Ocean, *Journal of Physical Oceanography*, *32*, 2882–2899.

Staquet, C., and J. Sommeria (2002), Internal gravity waves : from instabilities to turbulence, *Annu. Rev. Fluid Mech.*, *34*, 559–593, doi:10.1146/annurev.fluid.34.090601.130953.

Thorpe, S. A. (1966), On wave interactions in a stratified fluid, *J. Fluid Mech.*, *24*, 737–751.

Tobisch, E. (2016), *New Approaches to Nonlinear Waves*, lecture no ed., 309 pp., Springer Heidelberg.

Wunsch, C., and R. Ferrari (2004), Vertical Mixing, Energy, and the General Circulation of the Oceans, *Annual Review of Fluid Mechanics*, *36*(1), 281–314, doi:10.1146/annurev.fluid.36.050802.122121.

Yu, J., and L. N. Howard (2012), Exact Floquet theory for waves over arbitrary periodic topographies, *Journal of Fluid Mechanics*, pp. 1–20, doi:10.1017/jfm.2012.432.

Yu, J., and C. Mei (2000a), Do longshore bars shelter the shore?, *Journal of Fluid Mechanics*, *404*, 251–268.

Yu, J., and C. C. Mei (2000b), Formation of sand bars under surface waves, *Journal of Fluid Mechanics*, *416*, 315–348, doi:10.1017/S0022112000001063.

Zhao, Z., M. H. Alford, J. A. MacKinnon, and R. Pinkel (2010), Long-Range Propagation of the Semidiurnal Internal Tide from the Hawaiian Ridge, *Journal of Physical Oceanography*, *40*, 713–736, doi: 10.1175/2009JPO4207.1.